JGR Solid Earth

RESEARCH ARTICLE
10.1029/2018JB016941

Key Points:

- Most seismic ruptures remain confined to the reservoir interval, but under some conditions rupture outside of the reservoir can occur
- Rupture beyond the reservoir depth may occur for small fault offset, large stress drop, small fracture energy, and critical in situ stress
- The heterogeneous depletion-induced stress distribution around offset faults promotes nucleation of seismicity but limits rupture extent

Supporting Information:

- Supporting Information S1
- Data Set S1

Correspondence to:
L. Buijze,
loes.buijze@tno.nl

Citation:
Buijze, L., van den Bogert, P. A. J., Wassing, B. B. T., & Orlic, B. (2019). Nucleation and arrest of dynamic rupture induced by reservoir depletion. *Journal of Geophysical Research: Solid Earth*, *124*. https://doi.org/10.1029/2018JB016941

Received 30 OCT 2018
Accepted 15 FEB 2019
Accepted article online 18 FEB 2019

Nucleation and Arrest of Dynamic Rupture Induced by Reservoir Depletion

L. Buijze[1,2], P. A. J. van den Bogert[3], B. B. T. Wassing[1], and B. Orlic[1]

[1]Applied Geosciences, TNO, Utrecht, Netherlands, [2]HPT Laboratory, Department of Earth Sciences, Utrecht University, Utrecht, Netherlands, [3]Shell Global Solutions B.V. Rijswijk, Rijswijk, Netherlands

Abstract Seismic events induced by the depletion of hydrocarbon reservoirs can cause damage to housing and cause societal and economic unrest. However, the factors controlling the nucleation and size of production-induced seismic events are not well understood. Here we used geomechanical modeling of production-induced stresses and dynamic rupture modeling to assess the conditions controlling down-dip rupture size. A generic model of (offset) depleting reservoir compartments separated by a fault was modeled in 2-D using the Finite Element package DIANA FEA. Linear slip-weakening was used to control fault friction behavior. Fault reactivation was computed in a quasi-static analysis simulating stresses during reservoir depletion, followed by a fully dynamic analysis simulating seismic rupture. The sensitivity of reactivation and rupture size to in situ stress, dynamic friction, critical slip distance, and reservoir offset was evaluated. After reactivation, a critical fault length was required to slip before seismic instability could occur. In a subsequent fully dynamic analysis the propagation and arrest of dynamic rupture was simulated. Rupture remained mostly confined to the reservoir interval but could also propagate into the overburden and underburden or sometimes transition into a run-away rupture. Propagation outside the reservoir interval was promoted by a critical in situ stress, a large stress drop, a small fracture energy, and no or little reservoir offset. With increasing offset (up to the reservoir thickness), reactivation was promoted but dynamic rupture size decreased.

Plain Language Summary Gas production can cause earthquakes, which can be felt at the Earth's surface. Even though these earthquakes are relatively small, they can sometimes cause damage to housing and infrastructure which may have large societal and economic impact. An example of this problem are the earthquakes in the Groningen gas field in the north of the Netherlands, where the damages due to induced earthquakes have led to a production cap and early phase-out of gas production. An important question is how the earthquakes are made, and how large the earthquakes may become. Here we modeled the production-induced earthquakes with geomechanical modeling, which calculates the effect of gas production (pressure changes) on the forces (stresses) in the subsurface. These altered stresses can exceed the strength of preexisting faults in the subsurface, causing the fault to *break* and generate an earthquake. The modeling results showed that earthquake size depended on many factors such as the initial stress in the reservoir and the fault behavior. The earthquakes often remained confined within the gas producing interval. The geometry of the gas reservoir and faults played a large role in generating the earthquake. Results are consistent with field observations and help to understand the timing, location, and size of seismic events.

1. Introduction

Production-induced seismicity can cause damage to housing and infrastructure and have significant societal and economic impact, in particular in densely populated areas. One prominent example is the Groningen field in the Netherlands, where damage and unrest due to induced seismicity have led to a premature phase out of the gas production (e.g., van Thienen-Visser et al., 2015). To assess the hazard from induced seismic events, knowledge about the mechanisms, as well as the likely location, magnitude, and magnitude distribution of the induced events, is key. In particular, it is important to assess whether seismic events remain mostly confined to the reservoir interval or whether they can nucleate and/or propagate outside of the reservoir interval.

The production of gas from porous reservoir formations in the subsurface causes (i) a reduction of pressure (pressure depletion) and (ii) subsequent compaction (volume reduction) of the depleting reservoir. Past studies show that the decrease in pressure causes a reduction in reservoir volume, which results in stress changes within and around the reservoir, so-called poroelastic stressing (Hettema et al., 2000; Segall, 1989; Segall et al., 1994; Segall & Fitzgerald, 1998), and also in subsidence at the Earth's surface, which may be significant depending on the compressibility of reservoir rock, the depth, thickness, and areal extent of the reservoir (Hough & Page, 2016; van Thienen-Visser et al., 2015; Yerkes & Castle, 1976). Poroelastic stress changes on preexisting faults within and around the depleting reservoir can bring those faults to failure so that fault slip can occur, depending on the tectonic stress regime and the location and orientation of those faults (Orlic & Wassing, 2012; Segall, 1989). Shallow surface faulting may also occur at the edges of subsidence bowls in cases of significant subsidence (Yerkes & Castle, 1976). The extraction of a large volume (mass) of hydrocarbons could also cause triggering of deep earthquakes below the reservoir (Segall, 1985). Geomechanical modeling studies show how particular geometries such as production from reservoir compartments offset by a fault can locally enhance the stress changes and promote fault slip within the reservoir (Haug et al., 2018; Mulders, 2003; Nagelhout & Roest, 1997; Orlic & Wassing, 2013; van den Bogert, 2015; Wassing et al., 2017; Zbinden et al., 2017). Of particular interest for seismic hazard is the possibility for the seismicity nucleating within the reservoir interval to propagate outside the reservoir. However, the majority of geomechanical modeling studies focused on the development of stresses and their effect on the onset of fault slip but for postfailure behavior often simplified fault behavior is used, for example, ideal-plastic fault slip or a quasi-static analysis of frictional weakening. When one is interested in the size and propagation of seismic events, understanding dynamic fault behavior, which simulates fast slip, is essential since it exerts a dominant control on both the nucleation of the seismic rupture and more importantly the propagation and arrest (termination) of seismic rupture.

In the framework of natural seismicity numerous modeling studies have investigated the earthquake source process, simulating dynamic fault slip through inclusion of a slip-dependent (e.g., Andrews, 1976; Harris & Day, 1997) or velocity-dependent decrease of fault friction (e.g., Ben-Zion & Rice, 1997; Lapusta et al., 2000; Okubo, 1989). Fully dynamic rupture simulations are the most computer intensive simulations, which solve the full elasto-dynamic equations and include the effect of inertia and radiated seismic waves on the rupture process. Such simulations are typically used to model single events in detail and investigate for example the effect of initial stress and stochastic stress variability (e.g., Day, 1982; Duan & Oglesby, 2006; Ripperger et al., 2007) on, for example, fault slip rate, rupture velocity, and radiated waves. In particular, some of these studies investigated the conditions under which ruptures will arrest, which is important and useful in the light of analyzing (induced) earthquake sizes. A sharp transition is observed from arrested rupture (where only a small part of the fault ruptured) to runaway rupture in which the rupture continues indefinitely (Galis et al., 2015; Ripperger et al., 2007). This transition is favored by a critical initial stress state and/or large friction drop but also depends on the nucleation procedure used to initiate the dynamic models (Galis et al., 2015) and the distribution of stress heterogeneity over the fault (Ripperger et al., 2007).

Nucleation of rupture in the aforementioned models is mostly simulated in an artificial manner, for example, using a prescribed overstressed asperity as the nucleation zone (Galis et al., 2015). Besides artificial nucleation, other simplifications in the dynamic models include a uniform initial normal and shear stress, simplified planar geometry, and uniform elastic properties. Production-induced earthquakes on the other hand will nucleate due to specific production-induced stresses, which are spatially variable on faults. The locally perturbed fault stress will influence rupture nucleation and propagation. For induced seismicity recently a number of studies have used fully dynamic simulation of rupture, in the framework of injection (Cappa & Rutqvist, 2012; Jin & Zoback, 2018; Pampillón et al., 2018; Urpi et al., 2016) or production (Buijze et al., 2017; Wassing et al., 2017). However, the conditions leading to induced rupture nucleation and rupture arrest in depleting gas fields have not been investigated for a broad range of parameters and reservoir geometries.

This study investigates the nucleation and size of production-induced earthquakes, and in particular their propensity to propagate far outside of the producing reservoir interval, by modeling the stress changes due to production-induced seismicity, nucleation of the seismic instability, and propagation and arrest of dynamic rupture in a single model workflow in a 2-D Finite Element model (DIANA FEA). The modeling study was based on the Groningen gas reservoir in the Netherlands (Spetzler & Dost, 2017; van Thienen-Visser et al., 2015). Production from one or two compartments separated by a fault with or without offset was modeled quasi-statically in a 2-D model. The depletion-induced stress changes drive

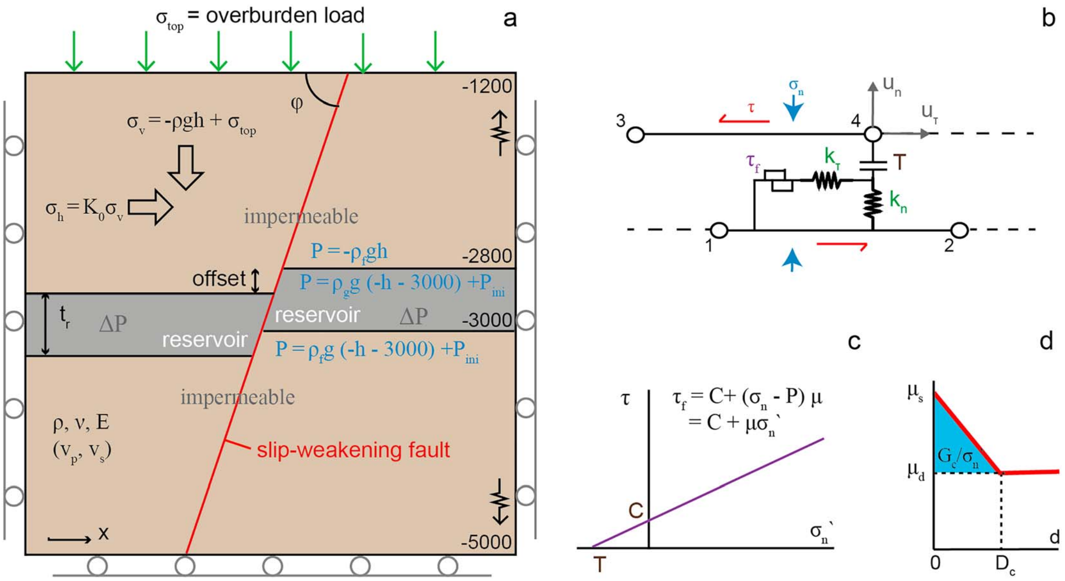

Figure 1. Model setup description of the interface elements used to model the fault, and the fault friction properties. (a) Geometry of the 2-D plane-strain model simulating a slip-weakening fault offsetting a producing reservoir formation. The model box is centered around the reservoir fault section. σ_{top} = simulated overburden weight, σ_{y} = vertical stress, h = depth, K_0 (=$\sigma_{\mathrm{h}}/\sigma_{\mathrm{v}}$) = stress ratio, and φ = fault dip. Elastic parameters are uniform across all formation (E = 15 GPa, ν = 0.15, ρ = 2,400 kg/m^3), corresponding to a P wave velocity V_p of 2,568 m/s and an S wave velocity V_s of 1,645 m/s. A uniform pressure change ΔP was prescribed in the reservoir formation (one or both sides) to simulate production. (b) Schematic representation of an interface element with nodes (open circles), normal and shear displacements u_n and u_τ normal and shear stiffness k_n and k_τ, tensile strength T, and fault strength τ_{f}. (c) Mohr Coulomb friction with fault strength τ_{f}, cohesion C, effective normal stress σ_n', pore pressure P, and friction coefficient μ. (d) Slip-weakening friction with shear slip d (relative plastic shear displacement across the fault), with static friction coefficient μ_s, dynamic friction coefficient μ_d, critical slip distance D_c, and fracture energy G_c.

reactivation of the fault, aseismic slip, and nucleation of the seismic instability. Linear slip-weakening friction was used to simulate fault behavior and seismic slip. Sensitivity analysis of reactivation and nucleation to the in situ stress, friction parameters, and reservoir offset was conducted. In the subsequent dynamic analysis rupture propagation and arrest were modeled, and sensitivity of the along-dip size of the dynamic event and potential of transition to runaway rupture to in situ stress, friction parameters, and reservoir geometry was analyzed.

2. Numerical Model Setup, Input Parameters, and Modeling Procedure

Depletion-induced stress changes, the subsequent nucleation and propagation of seismic rupture, and associated wave propagation into the subsurface were simulated in a 2-D plane-strain model setup using the general-purpose Finite Element package DIANA FEA v. 10.1 (DIANA 10.1 User Manual, 2016). In the following sections the model setup, governing equations, numerical considerations, and the input parameters are presented. The model input parameters were based on the Groningen field lithologies.

2.1. Governing Equations, Assumptions, and Modeling Workflow

The model space is a rectangular box centered around the intersection of a 70° dipping fault with a 200-m-thick reservoir formation (Figure 1a). The modeling procedure consists of three phases: (1) stress and pressure initialization, (2) quasi-static reservoir depletion and nucleation of seismic slip, and (3) fully dynamic rupture simulation. The key governing equations and assumptions used in these phases are briefly listed in the following.

During the first two phases the static equilibrium equation that is solved is

$$\nabla\cdot\boldsymbol{\sigma} + \boldsymbol{F} = \nabla\cdot\left(\boldsymbol{\sigma}' + \alpha P\right) + \boldsymbol{F} = 0, \tag{1}$$

with the total stress tensor $\boldsymbol{\sigma}$, the effective stress tensor $\boldsymbol{\sigma}$\`, the body forces $\boldsymbol{F}$ (including gravity), and Biot's coefficient α, and pore pressure P. The kinematic relationship between the strain vector $\boldsymbol{\varepsilon}$ and displacement vector $\boldsymbol{u}$ is

Table 1
Model Parameters for the Base Case Scenario

Base case values: Rock mass		Base case values: Fault	
Young's modulus E (GPa)	15	Dip φ (°)	70
Poisson's ratio ν (−)	0.15	Normal stiffness k_n (GPa)	150 (15)[a]
Density ρ (kg/m^3)	2,400	Shear stiffness k_s (GPa)	65 (6.5)[a]
Density gas in reservoir ρ_g (kg/m^3)	200	Static friction μ_s (−)	0.6
Initial gas pressure reservoir 3000 m depth (MPa)	35	Dynamic friction μ_d (−)	0.45
Density fluid overburden and underburden ρ_f (kg/m^3)	1,150	Critical slip distance D_c (m)	0.005
Stress ratio $K_0 = \sigma_h/\sigma_v$ (−)	0.75	Cohesion C (MPa)	0
Biot coefficient α (−)	1		

Note. Elastic parameters from Sanz et al. (2015).
[a] The values between brackets indicate the interface element stiffness values used in the fully dynamic analysis where the stiffness is set 10 times lower ($f_k = 1$) than in the quasi-static analysis ($f_k = 10$).

$$\boldsymbol{\varepsilon} = \frac{1}{2}\left[\nabla\mathbf{u} + (\nabla\mathbf{u})^T\right] \tag{2}$$

Linear elastic is assumed in the formations, with the constitutive equation (Hooke's law)

$$\boldsymbol{\sigma} - \alpha P = \boldsymbol{C} : \boldsymbol{\varepsilon} \tag{3}$$

where $\boldsymbol{C}$ is a fourth-order elasticity tensor. For an isotropic material this becomes

$$\boldsymbol{\sigma} - \alpha P = \frac{E}{(1+\nu)}\left(\frac{\nu}{(1-2\nu)}tr(\boldsymbol{\varepsilon}) + \boldsymbol{\varepsilon}\right) \tag{4}$$

where E is Young's modulus and ν is Poisson's ratio (see Table 1 for elastic properties). Plane-strain conditions were assumed with displacement in the out-of-plane strains $\varepsilon_{xz} = \varepsilon_{yz} = \varepsilon_{zx} = \varepsilon_{zy} = \varepsilon_{zz} = 0$ and out-of-plane stress $\sigma_H = \nu\ (\sigma_h + \sigma_v)$. At the sides and bottom of the model space displacement boundaries are imposed with $u_x = 0$ at $x = 0$ and $x = 4{,}000$ m, and $u_y = 0$ at $y = -5{,}000$ m. At the top of the model a constant stress boundary was prescribed, $\sigma_{\text{top}} = 23.6$ MPa at $y = -1{,}200$ m, so that σ_v at the reservoir level was 66 MPa, in agreement with observations.

The fault strength was controlled by Mohr-Coulomb friction (Figure 1c)

$$\tau_f = C + (\sigma_n - P)\mu_s \tag{5}$$

where τ_f is the failure strength, σ_n is the normal stress, C is cohesion, and μ_s is the static friction coefficient. Once the criterion is exceeded the fault deforms plastically. The postfailure behavior was governed by linear slip-weakening (Ida, 1972), where μ decreases linearly as a function of shear slip d (the relative plastic shear displacement across the fault) from the static friction coefficient μ_s at $d = 0$ to the dynamic friction coefficient μ_d at $d \geq$ critical slip distance D_c (Figure 1d and Table 1). The equations were solved with a Newton-Rhapson solver. During the quasi-static depletion phase pressure load steps were prescribed until the fault started to slip plastically. The pressure step size was then reduced based on the number of iterations required for convergence, until numerical instability was reached. At this point a small additional pressure change (<0.1% of the initial reservoir pressure) was added to cause a disequilibrium, and the analysis was switched to a fully dynamic calculation, including inertial effects and Rayleigh damping. The equation of motion is given by

$$\nabla\cdot\boldsymbol{\sigma}\text{`} + \boldsymbol{F} = \varrho\ddot{\boldsymbol{u}} + a\varrho\dot{\boldsymbol{u}} \tag{6}$$

where $\ddot{\boldsymbol{u}}$ is the acceleration vector. The use of Rayleigh damping gives rise to the added rate-dependent term $a\dot{\boldsymbol{u}}$, where $\dot{\boldsymbol{u}}$ is the velocity vector and a is one of the Rayleigh damping parameters. The constitutive equation for linear elasticity including Rayleigh damping becomes

$$\boldsymbol{\sigma}' = \boldsymbol{C} : \varepsilon + b\boldsymbol{C} : \dot{\varepsilon} \tag{7}$$

where b is the second Rayleigh damping parameters. The elastodynamic equation was solved with explicit time integration. On- and off-fault no pressure changes were modeled during propagation of dynamic rupture. During the dynamic phase artificial Rayleigh damping was used to reduce high-frequency numerical noise (e.g., Duan & Oglesby, 2006), with $a = 0$ and $b = 0.1\Delta t$ (equation (S4)), where Δt is the time step. The displacement boundaries remained active during the dynamic phase; the modeled time of interest was much shorter than the time it took for the waves to reach the model boundaries and cause reflections.

2.2. Element Size, Time Step, and Damping

An automated model-generator was constructed to generate the plane-strain model geometry. The fault was modeled with interface elements (L8IF), which allow elastic deformation until the Mohr Coulomb criterion is reached (equation (5)). Elastic deformation was controlled by a normal stiffness k_n and shear stiffness and k_τ (Figure 1b), which could be related to the formation stiffness through the factor f_k, with $k_\tau = f_k\,G$ and $k_n = f_k\,E$, where G is the shear modulus. Interface elements should have a very high (in theory infinite) stiffness to simulate a fault zone with 0-m thickness. However, faults in nature have a finite width and f_k may be used to allow elastic shear and normal deformation on a fault zone of thickness w by setting $f_k = 1/w$ (Mulders, 2003). Here the default $f_k = 10$, which corresponds to w of 0.1 m as is typical for faults with an offset of 10–100 m (Beach et al., 1997; Childs et al., 2009). During the dynamic simulation phase the stiffness was reset to $f_k = 1$ to avoid rapid waves propagating along the fault zone (see further S3 and Figure S2). The linear slip-weakening relationship that governs postfailure faulting behavior leads to a minimum resolution constraint to capture adequately the seismic shear slip on the fault, see S1 (Day et al., 2005; Palmer & Rice, 1973). The interface element length Δy was chosen such that at least 15 elements were within the low-velocity limit of the process zone Λ_0 (equation (S1)), corresponding to an element size of 0.75–1 m for the default parameters in Table 1. This element size adequately resolved the process zone at higher rupture speeds by 4 or more elements (Figure S1d). Along the fault segments in the overburden and away from the reservoir formation the element size gradually increased to a maximum of 50 m. For conditions under which rupture propagated far into the underburden and overburden a more refined mesh was used. The formations were meshed with an linear quadrilateral elements, which coarsened away from the fault, bringing the total number of elements to ~40,000–80,000. The explicit dynamic analysis requires a minimum time step for convergence, which is related to the element size via the Courant-Friedrichs-Lewy criterion (see equation (S3)). Here a Courant-Friedrichs-Lewy number of 0.5 is used (e.g., Day et al., 2005; Fukuyama & Madariaga, 1998), which gives a time step of 2×10^{-4} s.

2.3. Initial Stresses and Pressures, Pressure Changes, and Input Parameters

The initial horizontal stresses were defined through the total stress ratio K_0 as $\sigma_h = K_0\,\sigma_v$. The initial pore pressure gradients (Figure 1a) were imposed assuming a saline water density ρ_f of 1,150 kg/m^3, a gas density ρ_g of 200 kg/m^3, and an initial gas pressure P_{ini} of 35 MPa at −3,000 m (van Oeveren et al., 2017). At the reservoir level this resulted in a hydrocarbon overpressure of 3 MPa with respect to the saline water gradient (4.6 MPa overpressure with respect to a fresh water gradient), which is a commonly observed value in the Northern Netherlands (Verweij et al., 2012). Pore pressures in the fault segments having a reservoir formation on one or both sides were assumed to be similar to the pore pressure of the reservoir formation. For the other fault segments the overburden or underburden pore pressure was prescribed. Depletion was modeled in a simplified manner; a uniform pore pressure changes ΔP was prescribed for the reservoir formation and adjacent fault segments, with gas flow not explicitly modeled. This assumption is based reservoir models of the Groningen field, which show relatively uniform depletion and no or little pressure differential across the faults (NAM, 2016; van Oeveren et al., 2017). No fluid flow occurred from the rocks or fault in underburden and overburden to the depleting reservoir. Pressure changes were coupled one way to stress changes, as the pore fluid (gas) is very compressible compared to the reservoir rock.

The default parameters are summarized in Table 1. A variable reservoir offset could be incorporated by adjusting the depth of the hanging wall (HW). Results for a 0- and 50-m offset reservoir are studied in detail, as most of the faults in the Groningen field have offsets varying between 0 and half the reservoir thickness (Buijze et al., 2017; Wentinck, 2015). The default K_0 was 0.75; however, the K_0 in the Groningen field is highly uncertain (van Eijs, 2015) and sensitivity of rupture nucleation and size to K_0 in the range of 0.7–

0.8 was investigated. A static friction coefficient μ_s of 0.6 was assumed, which is consistent with the steady state friction coefficient of Rotliegend sandstone fault gouges deformed at the in situ conditions of the Groningen field (Hunfeld et al., 2017). Representative values for μ_d and D_c are difficult to obtain from laboratory experiments. We chose D_c and μ_d such that the fracture energy G_c (Figure 1d) was consistent with that estimated for typical Groningen earthquakes with a slip of millimeter to centimeter (Kraaijpoel & Dost, 2013), which was 10^3–10^5 J/m^2 (Nielsen et al., 2016), and the stress drop was in the range of 0.1–10 MPa as observed thus far in Groningen (Kraaijpoel & Dost, 2013). For the base case a D_c of 5 mm and a μ_d of 0.45 were used, which gives a G_c of 7,500 J/m^2 for a $\sigma_n{}'$ of 20 MPa. Sensitivities of rupture to μ_d (0.35–0.55) and D_c (1–100 mm) were analyzed.

2.4. Data Processing

The criticality of the fault was indicated with the Shear Capacity Utilization (*SCU*)

$$\mathrm{SCU} = \frac{\tau}{\tau_f} = \frac{\tau}{C + (\sigma_n - P)\mu_s}. \tag{8}$$

An *SCU* of 1 indicates that the fault element is at failure and can slip plastically in the normal direction, whereas an *SCU* of 0 indicates the absence of shear stress. Negative values are used in case the shear stress is positive in the reverse direction.

The pressure change at the onset of fault slip (fault reactivation) ΔP_r was defined as the pressure drop at which the shear stress on one of the fault element reached the shear strength τ_f ($SCU = 1$). To eliminate the effect of pressure load step size, ΔP_r was determined by fitting the evolution of *SCU* of the most critical fault element versus ΔP and compute at which ΔP an SCU of 1 was reached. After the onset of fault reactivation a phase of aseismic fault slip started in which incremental reservoir depletion ΔP_a was required to increase the size of the slipping fault patch. When the aseismic slip patch reached a critical size the aseismic nucleation phase ended at $\Delta P_n = \Delta P_r + \Delta P_a$. The corresponding along-fault length of the aseismic slip patch L_a at the end of the nucleation phase was termed L_n. The length of the subsequent seismic rupture L_s was determined by the length of the fault zone where slip rates (derivative of the relative plastic shear displacement across the fault) had exceeded 0.01 m/s.

3. Simulation Results

3.1. Seismic Rupture Induced on a Fault Crosscutting Two Depleting Reservoir Compartments Without Offset

This section describes the simulation results of seismic rupture induced by the depletion of a reservoir without offset, the simplest scenario in terms of geometry. The initial stresses and depletion-induced stress changes are presented and are compared to analytical solutions of linear poroelasticity. The aseismic nucleation process is shown and compared against a theoretical estimate for the critical nucleation length, and simulation results for the evolution of the subsequent seismic event are described.

3.1.1. Depletion-Induced Stresses on the Fault and Comparison to Analytical Solutions

The initial fault stresses in the reservoir interval, as well as in the overburden and underburden, were not (close to) critical. For the in situ stress ratio K_0 of 0.75, the initialized effective normal stress $\sigma_n{}'$ and shear stress τ on the fault at the reservoir depth interval were 15–17 MP and 6 MPa, respectively (dark lines in Figure 2). The overpressure resulting from the presence of the hydrocarbon column in the reservoir was manifested in the steplike 3-MPa increase in pore pressure at −2800 m (Figure 2a) and the corresponding decrease in $\sigma_n{}'$ (Figure 2b). The proximity to failure as given by the *SCU* (see equation (1)) ranged from 0.5 at the base of the reservoir to 0.6 at the top (Figure 2e) and signified that the fault was far from failure ($SCU = 1$). In the overburden and underburden the initial *SCU* was 0.5.

Depletion resulted in more critical fault stresses in the reservoir interval. The uniform reduction of pore pressure in the reservoir formations (Figure 2a) caused the effective normal stress and the shear stress on the fault to increase linearly with depletion (Figures 2b and 2c). The combined effect of the increasing stresses was a linear increase in *SCU*, until fault reactivation occurred at −29.95 MPa (Figure 2e). The corresponding stress path for a point on the fault within the reservoir interval (at −2,807-m depth) is shown in a Mohr-circle

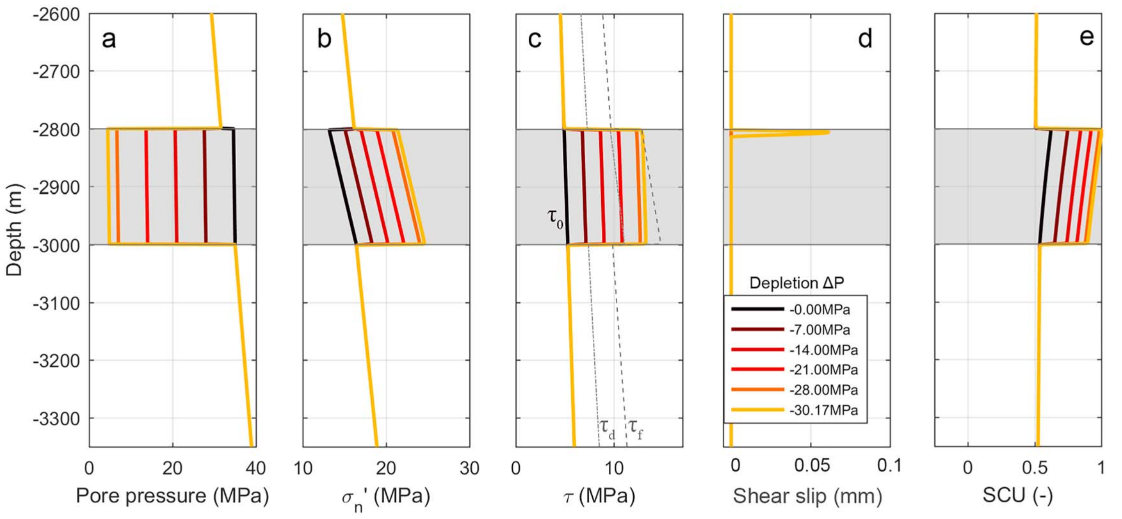

Figure 2. On-fault data for depletion of a reservoir without offset (fault dip φ 70°). (a) Pore pressure, (b) normal effective stress, and (c) shear stress. The failure shear stress τ_f and dynamic shear stress τ_d at $\Delta P = -30.17$ are shown by the dashed and dotted grey lines, (d) (Relative) Shear slip displacement and (e) the Shear Capacity Utilisation as a function of depth along the fault for a reservoir without offset and for different depletion pressures ΔP, as indicated by the legend in (d). The gray areas indicate the depth interval of footwall and hanging wall reservoir formations.

diagram (red circles in Figure 3). The initial and final states of stress are shown for reference (orange circles). The pressure drop caused the Mohr circle to shift to higher effective stresses but simultaneously caused the differential stress to increase. This increase was the result of a decrease in total horizontal stress with decreasing pressure (see also equation (S3)), while the total vertical stress remained constant. The increase in differential stress caused the fault stress to converge toward the failure line and become more critical (increasing *SCU*). The increase in *SCU* was uniform over the entire reservoir interval, whereas outside of the reservoir interval the fault stresses and the *SCU* were not affected by depletion.

The simulation results for fault reactivation agree well with the analytical solution for a laterally extensive depleting reservoir undergoing uniaxial compaction (e.g., Fjaer et al., 2008; Hettema et al., 2000). To compare between numerical simulation results and the analytical solution, we defined stress path parameters

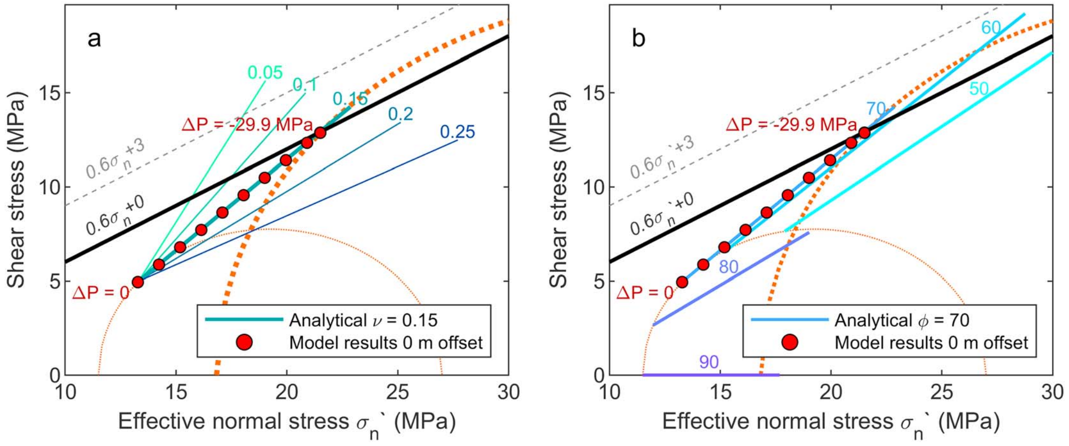

Figure 3. Effect of Poisson's ratio ν and dip angle φ on stress paths on the fault for depletion of a 0-m offset reservoir: numerical results and analytical solutions. The stresses on the fault are resolved at 2,807-m depth. The Mohr Coulomb failure line is shown as the black solid line; the grey dashed line indicates Mohr Coulomb failure including 3-MPa cohesion. The model results for reservoir depletion from $\Delta P = 0$ (initial stress state) to fault reactivation $\Delta P_r = -29.95$ are indicated by the red solid circles, and corresponding initial and reactivation states of stress are shown by the thin orange dotted semicircle and the fat orange dotted semicircle. (a) Effect of Poisson's ratio ν on the on-fault stress path. The analytical stress path corresponding to the model results ($\nu = 0.15$) is plotted with the dark cyan line. Analytically computed stress paths for other ν (0.05, 01, 0.2, and 0.25) are shown for reference, for a depletion $\Delta P = 0$ to $\Delta P = -35$ MPa (full reservoir depletion at 2,807-m depth). (b) Effect of fault dip φ on the on-fault stress path. The analytical stress path corresponding to the model results ($\varphi = 70°$) is plotted with the lilac line. Analytically computed stress paths for other φ (50°, 60°, 80°, and 90°) are shown for reference, for a depletion $\Delta P = 0$ to $\Delta P = -35$ MPa.

γ_n and γ_t, which are the changes in effective normal stress and shear stress on the fault plane as a function of depletion pressure ΔP (for derivation see S2)

$$\gamma_n = \frac{\Delta\sigma'_n}{\alpha\Delta P} = 0.5\gamma_h(1 + \cos 2\theta) - 1 \tag{9}$$

and

$$\gamma_\tau = \frac{\Delta\tau}{\alpha\Delta P} = -0.5\gamma_h \sin 2\theta \tag{10}$$

where θ (=90-fault dip φ) and γ_h is the horizontal stress path parameters (equation (S1))

$$\gamma_h = \frac{1-2\upsilon}{1-\upsilon} \tag{11}$$

which is a function of Biot coefficient α and Poisson's ratio ν. Dividing equation (10) with equation (9) gives slope of the stress path β in the Mohr diagram

$$\beta = \frac{\Delta\tau}{\Delta\sigma'_n} = \frac{-0.5\gamma_h \sin 2\theta}{0.5\gamma_h(1 + \cos 2\theta) - 1} \tag{12}$$

and the pressure drop at which reactivation occurs ΔP_{cr} (stress path intersects the failure line) is given by

$$\Delta P_{cr} = \frac{C - \tau_{\text{ini}} + \sigma'_{\text{nini}}\mu_s}{\gamma_\tau - \gamma_n\mu_s} \tag{13}$$

where τ_{ini} and σ_{nini} are the initial shear and normal stresses on the fault plane and C is the cohesion. For the base case ν of 0.15, φ of 70°, and μ_s of 0.6 the resulting slope of the stress path β is 0.970, and the reactivation pressure is −29.8 MPa. The fact that $\beta > \mu_s$ indicates convergence with the failure line (a destabilizing stress path), and because ΔP_{cr} is smaller than the intial reservoir pressure P_{ini} reactivation can occur as a result of poroelastic stressing. In the simulations the stress path had a slope of 0.968, which is a small difference (<0.2%) with respect to the analytical solutions. Reactivation occurred at a ΔP of −29.95 MPa, which is 0.5% more than the analytical solution. Differences between the analytical and numerical results may arise from elastic deformation on the interface elements, and it is important to set the stiffness parameters appropriately (see S3 and Figure S2).

The analytical solutions give basic insights into how the key factors Poisson's ratio and fault dip affect the stress path and potential for reactivation for the zero offset fault scenario. Poisson's ratio ν strongly affects the slope of the stress path β; the smaller the Poisson's ratio the steeper the stress path and the more unstable the stresses (Figure 3a). The calculated β (equation (12)) varied from 1.8 if $\nu = 0.05$ to 0.52 if $\nu = 0.25$. The onset of fault slip will not occur at any (theoretical) depletion pressure if the stress path does not intersect the Mohr-Coulomb failure line ($\beta \le \mu_s$), which was found for a Poisson's ratio equal to or larger than 0.22. The fault dip angle φ influenced three factors: (i) the initial stress on the fault and proximity to failure, (ii) the length of the stress path for a given pressure drop, and (iii) the slope of the stress path β (Figure 3b; van den Bogert, 2015). First, the fault dip determined the initial stress on the fault. The initial fault stress was most critical for a fault dip φ of 59°, that is, the tangent to the failure line atan (μ_s). The proximity to failure decreased for lower and higher dips. The base case fault dip of 70° was thus not the dip most critical at the initial conditions. Second, a decreasing fault dip resulted in a longer stress path. This was predominantly the effect of an increase in γ_n with decreasing fault dip (equation (9)). Third, the slope of the stress path had a nonlinear relation with fault dip angle, with a minimum of 0 at a fault angle of 0° and a maximum of 0.98 at a fault angle of 67°. The slope of 0 showed that reservoir depletion does not cause any shear stress on a vertical fault plane intersecting a reservoir without offset, irrespective of the value for Poisson's ratio. Which dip was most prone to reactivation depended on the combination of the initial stress state and the fault friction properties, the slope of the stress path, and the Poisson's ratio.

For the current study zero cohesion was assumed on the fault. However, at the shallow depths and resulting low stresses a small amount of cohesion may have a large effect on the reactivation potential, for example, 3-MPa of cohesion would require an unrealistically low Poisson's ratio for reactivation (Figure 3a).

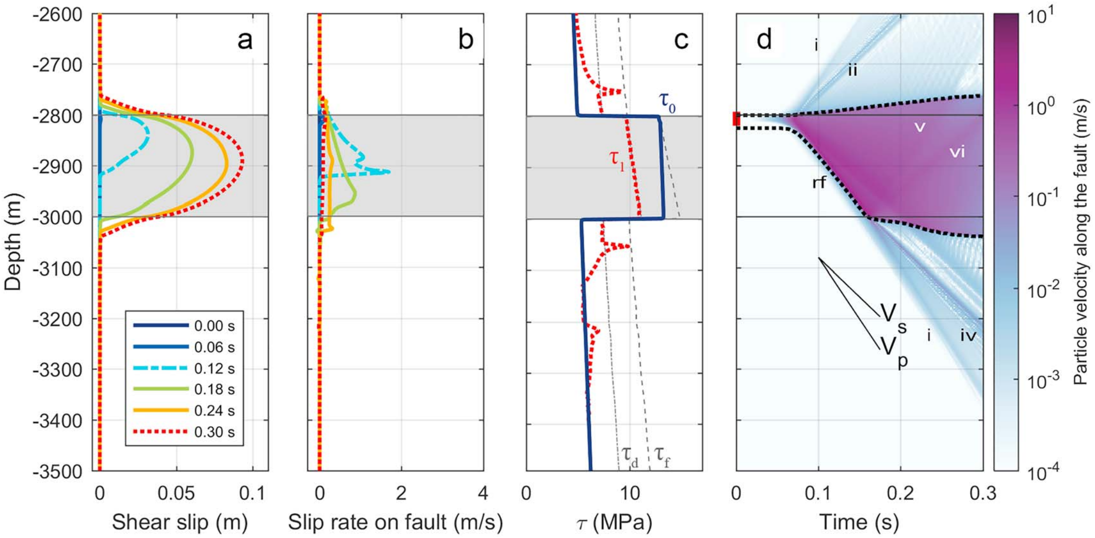

Figure 4. Simulation results for on-fault slip, slip rate, shear stress, and particle velocities during dynamic rupture on a 0-m offset fault. . The depth interval of the reservoir compartments is indicated by the shaded area. Model parameters $K_0 = 0.75$, $\mu_d = 0.45$, and $D_c = 5$ mm. (a) Shear slip as a function of depth along the fault for different points in time. (b) On-fault slip rates as a function of depth along the fault for different points in time. (c) Shear stress as a function of depth along the fault, for $t = 0$ s (dark blue line) and $t = 0.30$ s (red dotted line). The failure stress τ_f (gray dashed line) and dynamic shear stress τ_d (gray dotted line) are shown. (d) Fault-parallel particle velocities along the fault with time. The upper and lower limits of the seismic slip zone are indicated by the dotted black line; outside of this line all the motions are elastic. Particle velocities indicate different waves generated y the rupture with (i) *P* wave generated by nucleation on the rupture, (ii) *S* wave, (iii) mother rupture, (iv) *S* wave emitted by arrest of daughter rupture, (v) reflected *P* wave, and (vi) reflected *S* wave; rf, rupture front.

3.1.2. Fault Reactivation and the Onset of Seismic Rupture

Fault reactivation occurred at the top of the reservoir (−2,807 m) at a depletion pressure ΔP_r of −29.95 MPa (Figure 2e). After reactivation plastic slip on the fault occurred an aseismic slip patch developed at the top of the reservoir, growing in size as more and more fault elements were reactivated (Figure 2d). The aseismic slip patch increased until at a nucleation pressure change ΔP_n of −30.18 MPa instability was approached, so-called snap-through behavior, where the increasing stresses due to depletion pressure could no longer be sustained. This signified the onset of unstable, seismic rupture. Upon reaching instability, the aseismic slip patch evolved to a L_n of 13 m, which was in agreement with a theoretical estimate for the critical nucleation length for linear slip-weakening friction L_{UR}. This length was derived analytically as the solution to an eigenvalue problem and depends on the slope of the frictional weakening diagram, or weakening rate, $W = (\tau_f - \tau_d)/D_c$ (Uenishi & Rice, 2003)

$$L_{UR} = 1.158\,\frac{G}{(1-\nu)W} = 1.158\,\frac{GD_c}{(1-\nu)\left(\tau_f-\tau_d\right)}. \tag{14}$$

Here $G/(1-\nu)$ is the shear modulus for mode II and τ_f is the fault shear strength $\mu_s\sigma_n{}'$ and τ_d is the dynamic shear stress $\mu_d\sigma_n{}'$. The smaller D_c and/or the larger the strength drop $\tau_f - \tau_d$, the smaller L_{UR}. The theoretical critical nucleation length L_{UR} was computed for the simulation results using the average $\sigma_n{}'$ in the aseismic slip zone and was 13.8 m for the current scenario. The modeled L_n of 13 m corresponded closely to the theoretical L_{UR}, but not exactly because the L_{UR} was not an exact multiple of the element size of 1 m used in the model. The L_n is smaller than the fault length crosscutting the reservoir depth interval (220 m), and hence, seismic rupture could nucleate within the reservoir interval. At the onset of seismic rupture the stresses over the whole reservoir were close to critical with an *SCU* of 1 in the nucleation zone at the top of the reservoir, decreasing linearly to an *SCU* of 0.85 at the base of the reservoir (Figure 2e).

3.1.3. Dynamic Rupture Simulation and Evolution of Seismic Slip Length

After the critical nucleation size was reached during depletion, the subsequent evolution of seismic rupture was computed in a fully dynamic analysis.

Rupture propagated predominantly in the downdip direction from its nucleation site at the top of the reservoir (Figures 4a and 4d). Downdip propagation into the reservoir interval was favored by the fault stresses that were elevated during reservoir depletion and were close to the failure strength τ_f (Figure 4c). During the rupture the stress dropped by 2–3 MPa to its dynamic value τ_d within the slipping zone, whereas a stress concentration was present in front of the propagating rupture tip (see also Figure S1d). The rupture front (rf) reached the base of the reservoir after 0.12 s of slip and entered the underburden. In the underburden the in situ stress was far from its failure strength. In fact, the in situ stress in both the underburden and overburden was such that the static stress drop $\Delta\tau$ (=$\tau_0 - \tau_d$) was positive, which is inherently stabilizing. The stable stress state prevented significant updip propagation arresting the rupture at −2,753 m in the overburden and at −3,053 m in the underburden. In front of both rupture limits a shear stress concentration remained on the fault (Figure 4c). The total rupture length L_s along the fault was 326 m (=(−2,753–3053)/sin(70)), thus rupturing mainly the reservoir but also part of the overburden and underburden.

Rupture propagated in a crack-like manner; that is, slip increased at all locations within the seismic slip patch for the duration of the rupture (Figure 4a). The largest slip of 0.1 m occurred in the center of the slip patch, roughly in the center of the reservoir depth interval. Outside of the reservoir interval slip decreased rapidly as rupture was arrested. The simulated fault slip rates were largest at the crack tip and exceeded 4 m/s (Figure 4b), well into the seismic slip rate regime. Note that slip rate may be sensitive to cell size; however, total slip is not (see S1 and Figure S1).

The fault-parallel particle velocities (here taken from the HW side of the fault) are indicative for the seismic slip rate and seismic waves recorded along the fault zone (Figure 4). The dotted line shows the expansion of the seismic slip patch with time. Rupture expanded slowly for the first 0.03 s, and then accelerated, emitting a *P* and *S* wave (i and ii). High velocities in the order of 1 m/s were associated with the rf, as was also observed from the slip rate in Figure 4b. The downdip propagation speed of the rf (rupture velocity v_r) was constant in the reservoir interval, and nearly equal to the *P* wave velocity—that is, rupture was supershear. This can occur for Mode II ruptures where a stress peak develops ahead of the main rupture and nucleates a so-called daughter rupture propagating at intersonic velocity (Burridge-Andrews mechanism). The original mother rupture is also distinguishable, propagating at a velocity smaller than the *S* wave velocity (iii in Figure 4d), and it is visible as the second peak in slip rate at 0.12 s, at a depth of −2,880 m depth (Figure 4b). As the daughter rupture reached the base of the reservoir at −3,000 m it decelerated rapidly, reflecting a *P* and *S* wave upwards (v and vi), before being arrested at −3,010 m after 0.16 s. Meanwhile, the mother rupture continued to propagate downdip, and advanced the rf to −3,040 m before being arrested. Hence, supershear caused a relatively large rupture. Supershear is often related to Mode II and relatively critical prerupture stress (Dunham et al., 2011); whether this is likely in the shallow subsurface will be discussed further in section 4.

3.2. Seismic Rupture Induced on a Fault With 50 m

The previous section showed the results of the full analysis for a 0-m offset fault. Previous studies have shown that fault offset affects the stress changes during depletion and fault reactivation (Buijze et al., 2017; Mulders, 2003; Orlic & Wassing, 2013; Roest & Kuilman, 1994; van den Bogert, 2015). Here the effect of a reservoir offset of 50 m (a common offset in the Groningen field) on the depletion-induced fault stresses and fault reactivation (section 3.2.1) and dynamic rupture and final event size (section 3.2.2) is presented. Fault reactivation and rupture for other offsets is presented in section 3.4.

3.2.1. Depletion-Induced Stresses on a Fault With 50 m Offset

Reservoir offset did not significantly affect the initial fault stresses with respect to the 0-m offset case, and the initial state of stress was not close to critical (Figure 5). The initial effective normal stress in the reservoir was 14–17 MPa, and the 3 MPa overpressure resulting from the gas pressure was visible as stepwise decrease in pressure and increase in effective normal stress above −2,800 m (Figure 5b). The shear stress increased more linearly with depth, but contrary to the 0-m offset case showed small deviations from −2,800 to −2,850. Reservoir offset created a horizontal discontinuity in pressure across the fault, and hence a discontinuity in effective stresses, which caused small local variations in the initial stress field around the fault (see Figure S3). The resulting *SCU* decreased at the top of the reservoir depth interval was 0.6–0.65 with a peak at the top of the footwall (FW). The *SCU* decreased toward at the top of the reservoir depth interval to 0.5 at the base. Note that initial stresses may become more heterogeneous if elastic properties and K_0 vary per formation.

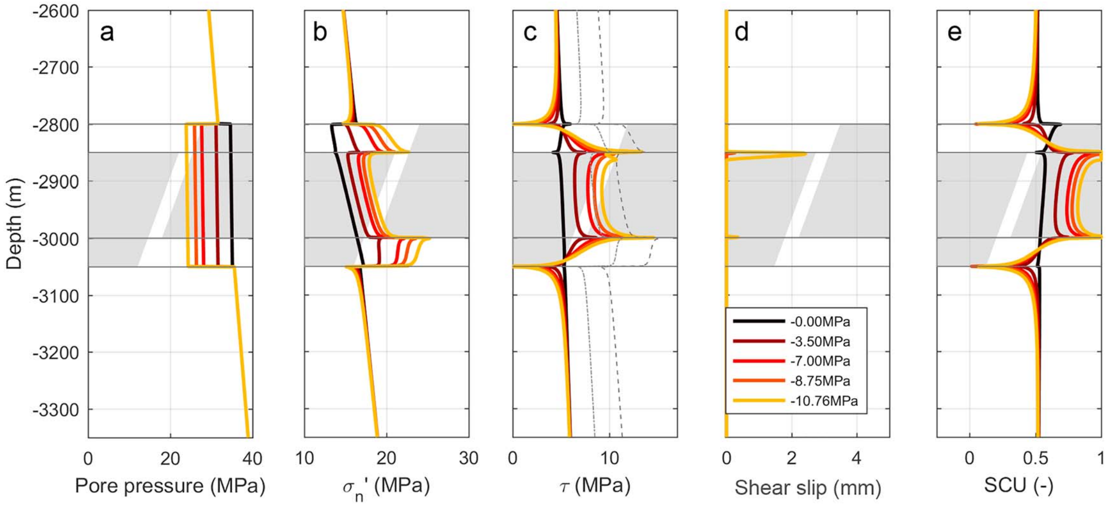

Figure 5. Simulated pressures, stresses, and plastic slip on the fault during depletion of two reservoir compartments with a 50-m offset. Simulation results are shown as a function of depth along the fault for different depletion pressures, as indicated by the legend in (d). The gray areas indicate the depth interval of footwall (right) and hanging wall (left) reservoir formations. (a) Pore pressure in the fault, (b) effective normal stress σ_n', (c) shear stress τ, (d) shear slip, and (e) the Shear Capacity Utilization.

Reservoir offset strongly promoted fault reactivation, as local stress concentrations developed during depletion. Both the effective normal stress σ_n' and shear stress τ increased with depletion, with the strongest increase in the interval where reservoir was juxtaposed against reservoir (−2,850 to −3,000-m depth; Figures 5b and 5c). The net effect of these stress increases was bringing this fault interval closer to failure —that is, the *SCU* increased (Figure 5e). The increases in the stresses and the *SCU* were amplified near the top of the HW (−2,850 m) and the base of the FW (−3,000 m). The shallowest of these two stress concentrations led to fault reactivation after a ΔP of −9 MPa. The peak stresses were then several MPa larger compared to the stress in the center of the juxtaposition interval (−2,925 m).

The criticality on the fault did not increase at every depth. The proximity to failure *SCU* decreased over the top 50 m of the FW and bottom 50 m of the HW, even though the shear stress increased over most of these intervals (Figure 5c). The shear stress increase in these intervals was small with respect to the effective normal stress increase. The normal stress caused a high fault strength so that the resulting *SCU* decreased, and the fault became more stable. The minimum SCU was found at the top of the FW (−2,800 m) and base of the HW (−3,050 m). The fault stress also stabilized outside of the reservoir depth intervals, because the shear stress decreased above the FW and below the HW. Hence, the offset reservoir geometry caused a heterogeneous stress distribution along the fault, with some regions becoming more critical and others more stable.

After a ΔP of −9 MPa fault reactivation occurred at the shallowest stress peak. This ΔP_r was three times less than for the 0-m offset reservoir ($\Delta P_r = -29.9$ MPa). The modeled slope of the stress path $\Delta\tau/\Delta\sigma_\mathrm{n}$ at the reactivation depth of −2,855 m was 1.6, which is much steeper and more unstable compared to the β of 0.97 for uniaxial conditions calculated in section 3.1.1. Hence, offset promoted failure and caused the stress evolution to deviate from the uniaxial conditions. The nonuniaxial conditions are also visible in the stress field around the offset fault, for example, in the local nonzero horizontal strains. The nonuniaxial conditions were dominant near the fault; more than one reservoir thickness away from the fault deformation became uniaxial (see Figure S3).

The aseismic slip patch that developed upon fault reactivation required a larger pressure drop to grow to its critical size than for the 0-m offset case. Beyond the reactivation pressure an additional ΔP_a of −1.8-MPa pressure was required to attain the critical nucleation length L_n of 11 m, at a ΔP_n of 10.8 MPa. The modeled L_n matched the theoretical critical nucleation length L_{UR}, which for this scenario was 12 m. Although L_n was similar to the L_n for 0-m offset reservoir, the amount of aseismic slip was 40 times larger as a result of the locally enhanced stresses, reaching a maximum of 2 mm of slip (Figure 5d). Aseismic fault slip reduced the friction in the center of the nucleation zone by 0.06, which equaled a reduction in shear stress of 1.3 MPa.

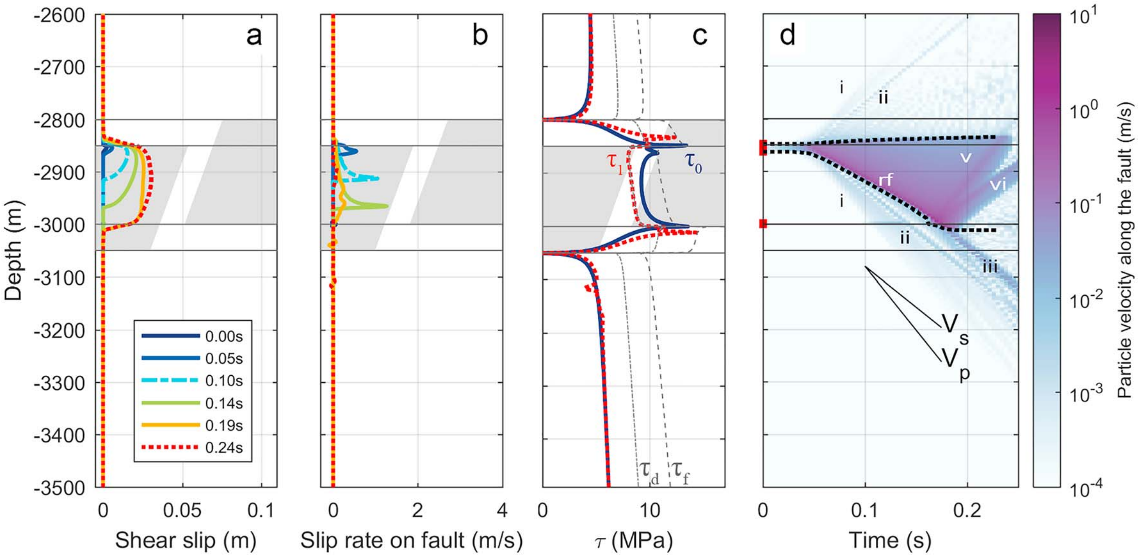

Figure 6. On-fault slip, slip rate and shear stress during dynamic rupture on a 50-m offset fault. Base case values of K_0 of 0.75, a μ_d of 0.45, and a D_c of 5 mm were used. The depth interval of the reservoir compartments is indicated by the shaded area. (a) Shear slip as a function of depth along the fault for different points in time. (b) On-fault slip rates as a function of depth along the fault for different points in time. (c) Shear stress as a function of depth along the fault for different points in time failure stress τ_f and dynamic shear stress τ_d computed at the start of rupture (at ΔP_n) is shown by the grey dashed line and grey dotted line. (D) Fault-parallel particle velocities along the fault with time. The upper and lower limits of the seismic slip zone are indicated by the dotted black line; outside of this line all the deformation is elastic. Particle velocities indicate different waves generated y the rupture with (i) *P* wave generated by nucleation on the rupture, (ii) *S* wave, (iii) mother rupture, (iv) reflected *S* wave, and (v) reflected *P* wave; rf, rupture front.

3.2.2. Dynamic Simulation of Rupture on a Fault With 50-m Offset

Rupture nucleated from the shallowest of two slip zones that developed during reservoir depletion, at −2,855-m depth (Figure 5). The slip patch expanded slowly for about 0.05 s, and then accelerated rapidly propagating primarily in the down-dip direction (Figures 6a and 6d). Downdip rupture was facilitated by the depletion-induced increased shear stress and related high *SCU* of 0.8–1 along the reservoir-reservoir juxtaposition interval (Figures 6c and 5e). After 0.18-s rupture reached the deeper stress concentration and was then arrested abruptly at the base of the FW at −3,010 m. Arrest occurred because rupture encountered a low shear stress region, which acted as a barrier. Stresses were stable at this location from −3,000- to −3,050-m depth (as well as at the top of the FW from −2,800- to −2,850-m depth) for two reasons. The relatively large effective normal stresses in these intervals (Figure 5b) were responsible for a high shear strength τ_f (Figure 6c). In addition, reservoir depletion had caused a reduction of the shear stress in these intervals (Figure 5c), so that the shear stress was far from failure, as also expressed by the low *SCU* of 0–0.5 (Figure 5e). Hence, the depletion from the 50-m offset reservoir caused stress peaks, which promoted nucleation of rupture, but at the same time had caused stress lows, which led to rupture arrest and prevented rupture from entering the underburden.

Rupture growth was crack-like, as for the 0-m offset scenario (Figure 6a). However, the rupture velocity was slower, and no supershear was observed. After 0.05 the rf (rf in Figure 6d) propagated downward at a constant rupture velocity of 1,275 m/s, which was 0.78 times the *S* wave speed of 1,650 m/s—that is, at subsonic rupture velocity. Hence, the arrival of the rf was preceded by the *P* and *S* waves emitted at the start of rupture (i and ii). The deeper stress peak at −3,000 m was dynamically triggered by the advancing rf, locally increasing the rupture velocity before abruptly deceleration and arrest of rupture at −3,010 m. *P* and *S* waves were emitted from rupturing of the −3,000-m stress peak and traveled upwards (v and vi), and rupture arrest also emitted *P* and *S* waves traveling downwards (iii).

Besides the rupture velocity, also the rupture length, total slip, and the slip rate were smaller than observed in the 0-m offset scenario. The final rupture had a size of about 180 m because it remained confined to the reservoir interval. A maximum slip of 0.03 m was attained at −2,900-m depth (Figure 6a). Seismic slip rates up to 2 m/s were observed, increasing as rupture propagated downward. Also, the stress drop was more variable than for the 0-m offset case due to the heterogeneous shear stress, ranging from 1 MPa in the center of

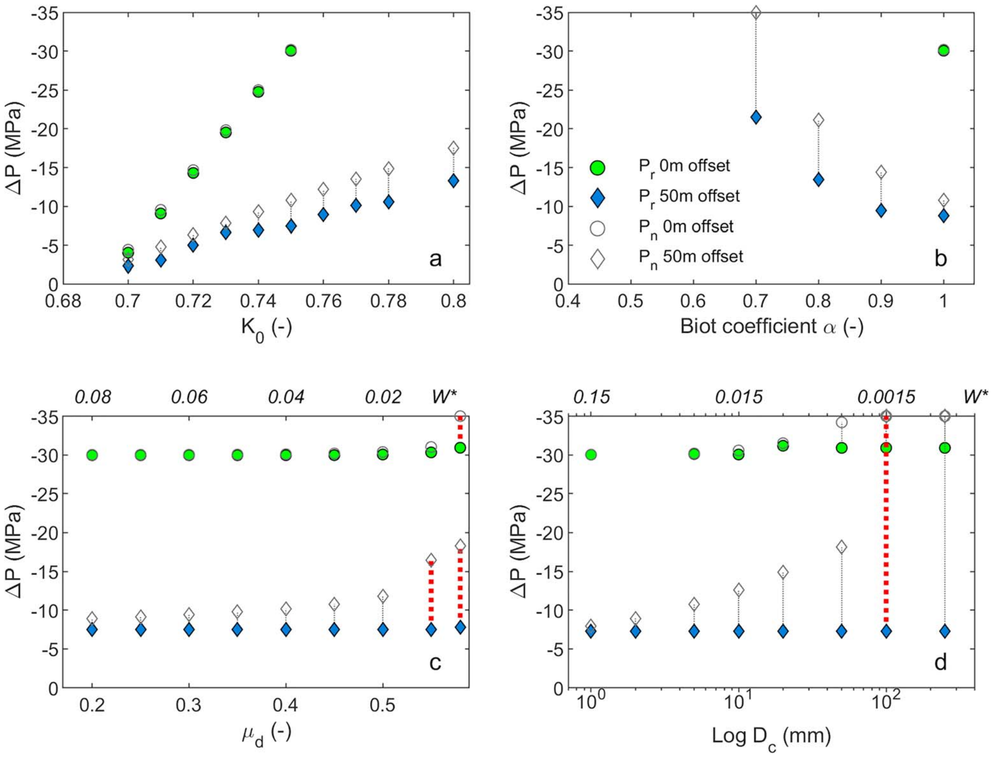

Figure 7. Sensitivity of reactivation pressure ΔP_r and nucleation pressure ΔP_n to various model input parameters. The lines connecting ΔP_r and nucleation ΔP_n show that aseismic pressure increment ΔP_a where the red dotted lines were used fault slip had exceeded the critical slip distance D_c. Unless otherwise specified, the base case input parameters for the sensitivity runs are $K_0 = 0.75$, $\mu_s = 0.6$, $\mu_d = 0.45$, and $D_c = 0.005$ m. Sensitivities of fault reactivation are shown for (a) initial state of stress K_0, (b) the Biot coefficient α, (c) the dynamic friction coefficient μ_d, and (d) critical slip distance D_c. The numbers shown above the graphs in c and d are the weakening rates $W^* = (\mu_s - \mu_d)/D_c$ corresponding to the different D_c and μ_d used, in mm^{-1}.

the reservoir interval to 5 MPa at the two stress peaks at −2,855 and −3,000 m. Reservoir offset thus resulted not only in different depletion-induced stress changes, but through these stress changes also resulted in different dynamic rupture characteristics and radiated waves.

To summarize, stresses developed by depletion of an offset reservoir promoted fault reactivation and rupture nucleation but led to a smaller event with lower rupture velocity and smaller slip and slip rates.

3.3. Effect of In Situ Stress and Friction Parameters

In this section we evaluate sensitivity of the fault reactivation and final rupture length to the in situ stress, and friction parameters, for 0- and 50-m reservoir offset.

3.3.1. Effect of In Situ Stress and Friction Parameters on Fault Reactivation (0- and 50-m Reservoir Offset)

The pressure required for reactivation (ΔP_r) and nucleation of instability (ΔP_r) increased linearly with increasing initial stress ratio K_0 (i.e., an increasingly stable in situ stress) for both the 0- and 50-m offset reservoirs (Figure 7a). At a stress ratio of 0.7 the fault was relatively close to failure, requiring a ΔP of −2 to −3 MPa for reactivation for both 50- and 0-m offset reservoir formations. For the 0-m offset the increase of reactivation pressure with the stress ratio was strongest, and at $K_0 > 0.75$ reactivation no longer occurred. However, for the 50-m offset formations reactivation occurred over the entire range of stress ratios, as the stress path was more critical due to the formation of stress concentrations (see section 3.2.1). At the most stable K_0 of 0.8 the required pressure change for reactivation was only about one third of the initial reservoir pressure. The pressure increment required to bridge the aseismic phase (ΔP_a) and the nucleation pressure also increased linearly with the stress ratio and was larger for the 50-m offset case than for the 0-m offset. The larger aseismic pressure increment for 50-m offset reservoirs resulted from a slower expansion of the aseismic slip patch for the peaked loading stresses, compared to the more uniform stress distribution for 0-m offset.

A decrease in Biot coefficient α required a larger pressure change for reactivation and nucleation (Figure 7b). The Biot coefficient controls the extent to which pressure changes translate into effective stress changes (equation (1)), and a lower Biot coefficient results in smaller fault stress path parameters (equations (9) and (10))) and hence requires a larger pressure change. For 0-m offset no reactivation occurred for $\alpha < 0.95$. For 50-m offset the relation between Biot and reactivation pressure was nonlinear, with reactivation becoming increasingly difficult at lower Biot values.

A larger dynamic friction μ_d and D_c (i.e., a lower weakening rate W^*, where $W^* = W/\sigma_n` = (\mu_s - \mu_d)/D_c$) did not affect the reactivation pressure but led to a larger aseismic pressure increment and higher pressure required for nucleation on instability (Figures 7c and 7d). Larger pressure changes are required to attain the critical nucleation length which increased with the lower W^* (equation (14)). For 0-m offset the aseismic pressure increment increased from −0.03 MPa ($\mu_d = 0.2$) to −0.7 MPa ($\mu_d = 0.55$), whereas for 50-m offset formation the aseismic pressure increment showed a stronger dependency on the dynamic friction, increasing from −1.5 MPa ($\mu_d = 0.2$) to −4.5 MPa ($\mu_d = 0.5$).

For some parameter combinations nucleation of instability did not occur, even though the fault was reactivated. This was observed in three different scenarios. First, it could be that the nucleation length could not be reached before full reservoir depletion ($\Delta P_n > \Delta P_{\mathrm{ini}}$). This occurred at, for example, Biot of 0.7 for the 50-m offset case (Figure 7b). Second, instability could not nucleate if the nucleation length was much larger than the reservoir interval—that is, the length over which the stress buildup occurred. This happened at a critical slip distance $D_c > 100$ mm, where the theoretical nucleation length L_{UR} was >300 m. Third, instability did not occur when aseismic slip in the nucleation zone d_a exceeded the critical slip distance ($d_a > D_c$; red dotted lines in Figure 7c and d). Upon further loading (pressure change) the aseismic slip patch continued to grow beyond the nucleation length. Other studies showed that still small instabilitities could occur under these conditions (Viesca & Rice, 2012), but under the current loading conditions no dynamic instability was observed for 0-m offset. For 50-m offset however, dynamic instability occurred even though $d_a > D_c$ ($\mu_d = 0.55$ and 0.58 in c), due to the merging of the shallower slip zone with the deeper slip zone at −3,000-m depth. Hence, merging of multiple slip zones related to the stress peaks that formed in the offset reservoir caused an additional possibility for the nucleation of instability.

3.3.2. Effect of In Situ Stress and Friction Parameters on the Seismic Rupture Length (0- and 50-m Reservoir Offset)

Here the sensitivity of the seismic rupture length to the in situ stress and friction parameters is presented for the 0-m offset and 50-m offset scenarios. Three different values for the dynamic friction were evaluated ($\mu_d = 0.35$, 0.45, and 0.55). For each μ_d three different weakening rates were analyzed ($W^* = 0.03$, 0.0075, and 0.0038 mm^{-1}). Particular attention is paid to the conditions that may cause so-called run-away ruptures, which is characterized by self-sustained rupture propagation far outside the reservoir depth interval toward the top and bottom surface of the model.

Rupture length L_s increased for lower dynamic friction coefficients—that is, larger stress drops. The largest rupture lengths were observed for the lowest dynamic friction coefficient of 0.35 (Figures 8a and 8d). Rupture propagation outside of the reservoir interval (shaded area) occurred with final rupture lengths of several hundreds of meters. Moreover, a transition to runaway rupture was observed toward the lower end of the in situ stress ratios evaluated. The rupture length and in situ stress at which the transition to runaway occurred (i) increased with the weakening rate W^* and (ii) decreased with the reservoir offset.

First, higher weakening rates W^* resulted in larger ruptures and a transition to runaway rupture at the higher (more stable) stress ratios. Runaway rupture was observed at a stress ratio $K_0 \leq 0.74$ for a weakening rate of 0.03 mm^{-1} and at $K_0 \leq 0.72$ for a weakening rate of 0.0038 mm^{-1} (Figure 8a). The lower weakening rate resulted in a longer nucleation length (equation (14)). The longer nucleation length caused the stress to drop to the dynamic value over a longer fault length during the aseismic phase, so less stress was available for rupture in the reservoir. Figure 9a shows, for example, how the nucleation zone covered half of the reservoir interval (red line on y axis) and how the initial expansion of rupture out of the nucleation zone was slow. Also, rupture did not transition to supershear within the reservoir interval. Additionally, the lower weakening rate cause a larger fracture energy G_c so that more energy was consumed by the fracture process, leaving less energy to propagate, thus resulting in smaller ruptures.

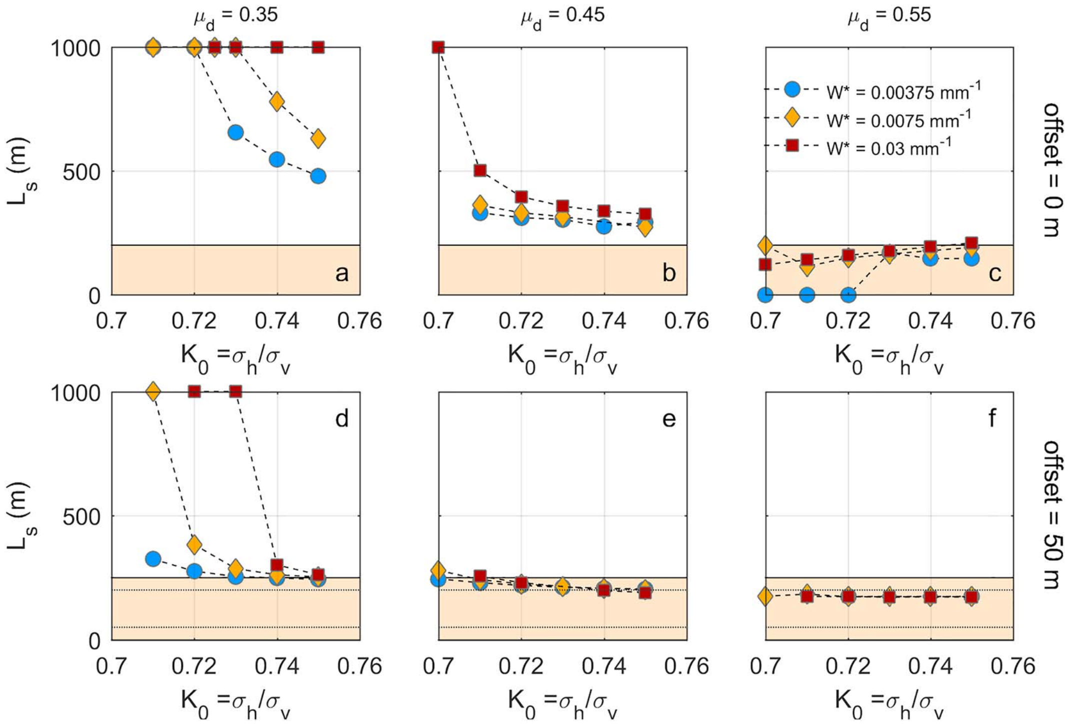

Figure 8. (a–f) Rupture arrest as a function of in situ stress K_0, dynamic friction coefficient μ_d, and weakening rate W^*. The symbols show the upper and lower limit of seismic rupture for 0-m offset (circles) and 50-m offset (diamonds) simulations. The shaded area indicates the reservoir depth interval, with dotted lines in (d)–(f) indicating the offset.

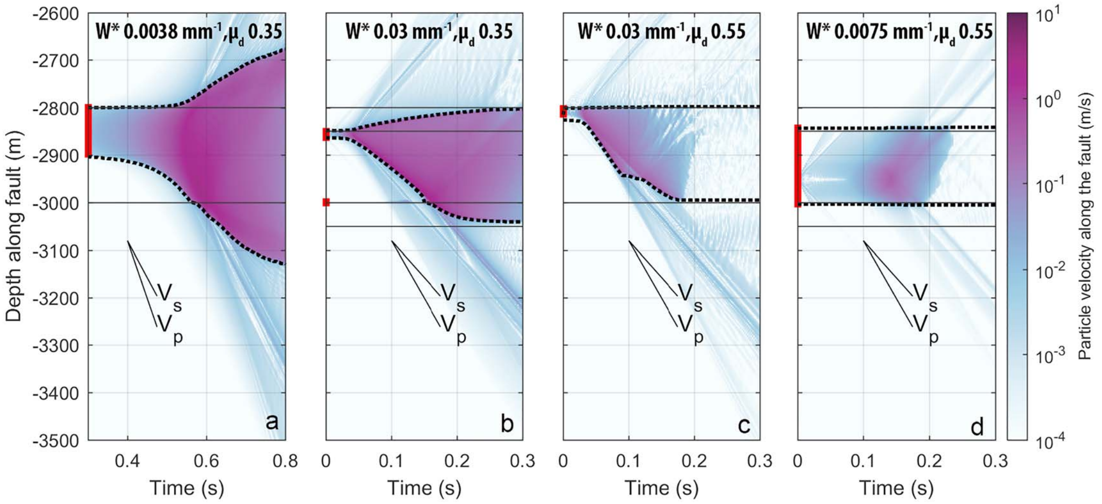

Figure 9. Rupture growth and wave propagation recorded on the fault for various W^* ($=W/\sigma_n'$) for 0 and 50-m offset reservoir compartments. The colors indicate the fault-parallel particle velocities recorded along the fault as a function of time. The black dotted lines show the boundaries of seismic slip patch as a function of time; within these lines plastic fault slip occurred. The horizontal solid lines outline the depth interval of the reservoir (footwall, 2,800- to 3,000-m depth), and the dashed lines outline the depth interval of the hanging wall for the 50-m offset case (2,850- to 3,050-m depth) The vertical fat red line plotted on top of the y axes shows the length of the fault that was slipping aseismically at the start of the seismic instability (L_n). For reference the P wave (V_p) and S wave (V_s) velocities are indicated in the plots. The K_0 was 0.75. Results are shown for (a) 0-m offset, $\mu_d = 0.35$, and $W^* = 0.0038$ mm^{-1}; (b) 50-m offset, $\mu_d = 0.35$, and W^* 0.03 mm^{-1}; (c) 50-m offset, $\mu_d = 0.55$, and W^* 0.03 mm^{-1}; and (d) 50-m offset, $\mu_d = 0.55$ and W^* 0.0075 mm^{-1}.

Second, the heterogeneous stresses formed during depletion of the 50-m offset reservoir compartments tended to confine ruptures to the reservoir, in particular for lower weakening rates (Figure 8d). Transition to runaway rupture did occur, but at a more critical in situ stress ratio than for the 0-m offset case, compare, for example, the difference between Figures 8a and 8d. At a stress ratio > 0.74 all ruptures remained confined to the reservoir. For example, at a stress ratio of 0.75 a subsonic rupture propagated downdip from the nucleation zone at −2,855 m (Figure 9b). The deeper stress peak was dynamically triggered, locally increasing the rupture velocity and emitting P and S waves upward and downward. However, abrupt arrest occurred at −3,050 and −2,800 m where depletion-induced stress was stable (see e.g., Figure 6c).

A higher dynamic friction coefficient of 0.45 caused smaller rupture lengths compared to runs with a dynamic friction of 0.35. Rupture propagation outside of the reservoir was only observed the 0-m reservoir offset (Figure 8b). For this offset rupture transitioned into runaway rupture only at the most critical in situ stress ratio explored ($K_0 = 0.70$). At higher stress ratios rupture was arrested, decreasing from 500 m ($K_0 = 0.71$) to 300 m ($K_0 = 0.75$). As in Figure 8a, high weakening rates promoted larger ruptures compared to low weakening rates. No rupture propagation outside the reservoir interval was observed for 50-m reservoir offset; again the stable depletion-induced stresses at the base of the HW and top of the FW acted as a barrier and limited rupture extent to 200 m for all stress ratios evaluated.

For the largest dynamic friction coefficient of 0.55 rupture did not propagate outside of the reservoir interval for any of the stress ratios considered. In the 0-m offset case rupture length decreased with decreasing stress ratio, contrary to previously observed dependencies on stress ratio. Inspection of the results indicated that at smaller stress ratios rupture propagated with subsonic velocities, whereas at larger stress ratios supershear occurred, which led to larger ruptures, for example, at a stress ratio of 0.75 (Figure 8c). The difference may be explained by the difference in stress drop. At a smaller stress ratio the in situ stress is more critical, so that the required increase in shear and effective normal stress for reactivation is small. At the onset of rupture the effective stress was relatively low, and hence, the stress drop was also low, which prevented a transition to supershear. For the 50-m offset case the rupture length remained constant at 180 m with in situ stress ratio. In many cases the critical slip distance was reached during the aseismic slip phase and instability occurred only due to merging of the two slip zones. This resulted in a relatively small and slow rupture event (e.g., Figure 9d). Despite rupture being slow, it did rupture the entire reservoir because a large part of the fault was already slipping and stresses had been lowered to the dynamic value during the aseismic slip phase (red line along y axis) according to the linear slip-weakening friction on the fault.

3.4. Effect of Various Reservoir Offset on Nucleation and Seismic Rupture

The previous sections focused on nucleation and seismic rupture induced by depletion of reservoir compartments without offset and with 50-m offset. Here the effect of various offsets on reactivation and final rupture size is presented.

3.4.1. Effect of Reservoir Offsets on Stress Path Parameters and Fault Reactivation

The influence of the reservoir offset on the stresses on the fault is shown by the *SCU* along the fault plane, and the normal and shear stress path coefficients γ_n and γ_τ respectively and their ratio $\beta = \gamma_\tau/\gamma_n$.

The *SCU* showed two peaks for all offsets at the onset of seismic rupture, except for an offset of 0 and 200 m (Figure 10). In the case without offset the absence of shear stress concentration causes reactivation at larger depletion pressure compared to cases with offset For normal offsets these peaks were located at the top of the HW and bottom of the FW reservoir. In the depth interval between the two peaks the SCU was also elevated with respect to the initial *SCU*. This high *SCU* interval reduced in size as offset increased and the *SCU* peaks at the top of the HW and bottom of the footwall approached each other. Concurrently, both the stress path parameters γ_n and γ_t (Figure 10b) and the slope of the stress path β increased (Figure 10c), which caused a reduction of reactivation pressure with offset (Figure 10d). At a reservoir offset equal to the reservoir thickness (200 m) the peaks coincided to form a single peak. The co-location of the two shear stress peaks resulted in the largest stress path parameters, and reactivation occurred at the smallest pressure drop. At a reservoir offset larger than the thickness again two stress peaks developed. Here nucleation occurred also at the shallow stress peak, which is now located at the bottom of the FW . Depletion also caused local lows in SCU at the top of the FW and at the bottom of the HW, for all normal offsets. These lows can act as barriers to propagating rupture (e.g., section 3.3.2).

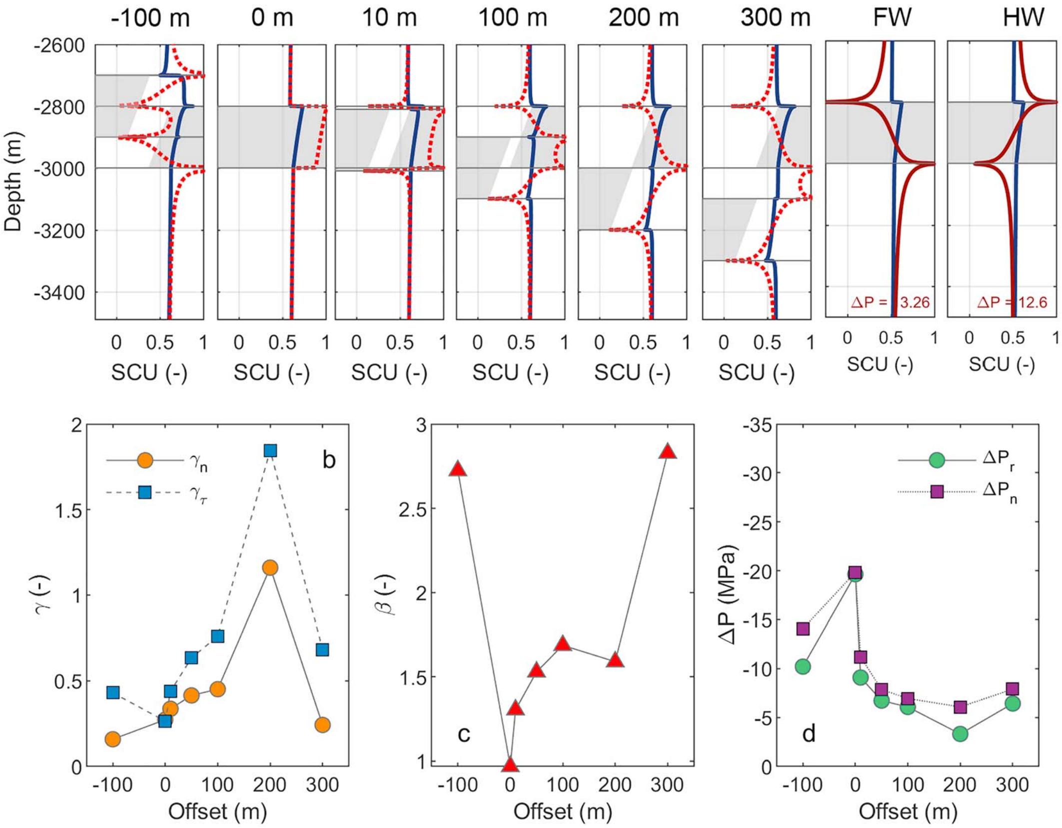

Figure 10. Effect of offset on fault stress, stress path, and pressure required for failure. (a) Influence of reservoir offset on the evolution of stress criticality (SCU) along a 70° dipping fault for an initial K_0 of 0.75. The dark blue line indicates the initial SCU; the red indicates line the state of stress when seismic instability occurred. The value at the bottom of the figures indicates the pressure required to reach this instability. The grey areas indicate on the left the depth interval of the hanging wall, on the right the depth interval of the footwall reservoir formation. The offsets are normal offsets indicated by the number above the figures. FW, depletion of the footwall only; HW, depletion of the hanging wall only. (b) Stress paths parameters γ_n $(=\Delta\sigma_n/\alpha\Delta P)$ and γ_τ $(=\Delta\tau/\alpha\Delta P)$ at the center of the reactivated slip zone for different formation offsets. (c) Stress path slope β at the center of reactivated slip zone for different formation offsets. (d) ΔP required for reactivation (ΔP_r) and nucleation (ΔP_n) for different offsets.

For a reverse offset the stress peaks still developed at the top of the HW and base of the FW. These now formed the deepest and shallowest parts of the reservoir interval. The stress lows were located between the stress peaks, rather than above and below. The stress path was relatively steep, but the stress path parameters were small, so the reactivation pressure was larger than for normal offsets.

When only the HW of FW were depleted, an asymmetric stress pattern developed with a single maximum at the top (HW) or the base (FW) of the reservoir and a single minimum at the opposite side. In fact, the stress pattern on a fault crosscutting two depleting formations is the superposition of the HW and FW cases. The asymmetric stresses may promote ruptures predominantly in one direction.

3.4.2. Effect of Reservoir Offsets on Rupture Length

Rupture length decreased with increasing reservoir offset, up to offsets equal to the reservoir thickness (Figure 11). For a dynamic friction of 0.35 runaway rupture was observed for the smallest offsets of 0, 10, and 50 m. For these offsets the length of the stable stress regions at the base of the HW and top of the FW was relatively small (see Figure 10a) and did not prevent rupture propagation outside of the reservoir. For larger offsets, the stable stresses had developed over a larger depth interval above and below the reservoir, effectively confining rupture to the reservoir interval. For example, for 100-m offset rupture was arrested at the base of the HW and propagated only a short distance above the top of the FW. For 200-m offset rupture was fully confined to the reservoir interval. At offsets larger than the reservoir thickness rupture length increased again, rupturing both reservoir depth intervals plus the depth section between the HW and the FW where a high SCU had developed (Figure 10). Ruptures were very large for depletion of only the HW or FW (reservoir bounding faults); only a single stress concentration and a single stress low formed

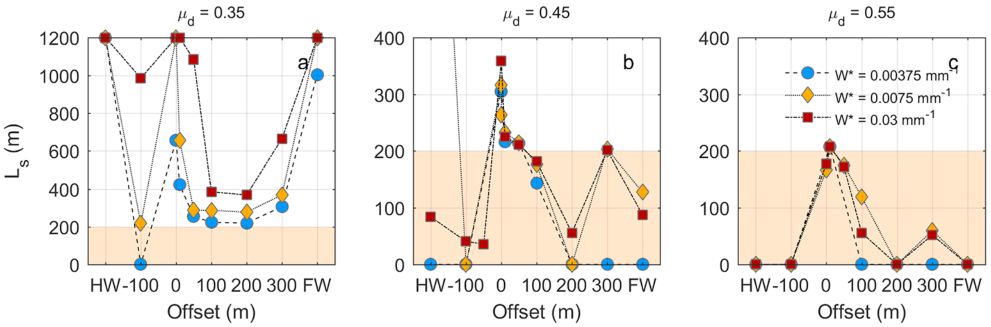

Figure 11. Rupture length L_s against reservoir offset for different dynamic friction values μ_d and weakening rates W^*. The in situ stress ratio $K_0 = 0.73$ for all runs; close to the transition to runaway rupture for the 0- and 50-m offsets at $\mu_d = 0.35$. The reservoir thickness is indicated with the shaded area. HW indicates depletion of the hanging wall only; FE indicates depletion of the footwall only. (a) L_s for $\mu_d = 0.35$, (b) L_s for $\mu_d = 0.35$, and (c) L_s for $\mu_d = 0.35$.

(Figure 10a) so that rupture propagation to respectively the overburden and underburden was easy. For the reverse offset a large rupture length was observed. In fact, the event consisted of two separate slip patches. Rupture nucleated at the deeper stress concentration and could propagate hundreds of meters into the underburden as no stress barrier formed during depletion (Figure 10). In addition, this rupture dynamically triggered the shallow stress concentration, which also ruptured and propagated upwards, adding to the total event size. This shows that dynamic effects can have a significant effect on rupture length.

Similarly, for a dynamic friction μ_d of 0.45 rupture length decreased with offset, but rupture lengths were smaller than for the dynamic friction of 0.35 (Figure 11b). Rupture was mostly confined to the reservoir interval, except for the 0-m scenario (L_s = 360 m) and depletion of the HW. For larger offsets rupture decreased to about the reservoir thickness of 200 m. Only a small part of the reservoir ruptured for the 200-m offset scenario, where a single stress peak had formed during depletion. Also, for a reverse offset of −100 m the event remained small as only the deeper stress concentration ruptured locally. No dynamic triggering of the shallow concentration was observed. With decreasing weakening rate rupture size became smaller, and for some offsets (−100, 200 m, HW, FW) no instability nucleated and only aseismic slip occurred, as the critical slip distance was attained prior to reaching the critical nucleation length.

Ruptures were smallest for a dynamic friction μ_d of 0.55 and decreased also with offset. For 0-m offset the entire reservoir ruptures, but only part of the reservoir ruptured for the 100-m offset and the 300-m offset (L_s 50–100 m depending on the weakening rate). For many runs aseismic slip occurred as D_c was reached during the nucleation phase.

To summarize, dynamic rupture size decreased with reservoir offset, increasing dynamic friction coefficient, and decreasing weakening rate (equivalent to increasing fracture energy or larger D_c).

4. Discussion and Implications

Understanding the potential for depletion-induced rupture to propagate outside of the reservoir interval is important to constrain (maximum) magnitudes that can occur as a result of reservoir production. Previous studies modeling depletion-induced seismic events often employed simplified faulting behavior to evaluate rupture size. However, it is important to include the depletion-induced stresses, as well as realistic dynamic faulting behavior to properly model rupture propagation. In this study we simulated reservoir stresses leading to fault reactivation and nucleation of seismic instability, and the subsequent fully dynamic rupture process using linear slip-weakening fault friction, which is often used to model natural earthquakes. The results showed that rupture mostly remained confined to the reservoir depth interval, but under some circumstances could propagate outside of the reservoir interval. A critical in situ stress, large friction drop, small fracture energy, and small reservoir offset promoted large ruptures exiting the reservoir interval. In the following we discuss modeling of poroelastic stressing and fault reactivation in the light of previous studies, the dynamic rupture length and propagation beyond the reservoir boundaries, and limitations and additional factors affecting rupture growth. Additionally, we discuss the implications for the Groningen field and more general implications for modeling of induced seismicity.

4.1. Production-Induced Stressing Causing Fault Reactivation and Nucleation of Rupture

Fault reactivation on faults offsetting two depleting reservoir formations was promoted with respect to faults without offset. This finding is in accordance with previous studies that also showed that fault offset and differential compaction enhanced reactivation (Mulders, 2003; Nagelhout & Roest, 1997; Orlic & Wassing, 2013; Roest & Kuilman, 1994; van den Bogert, 2015). Whereas the depletion-induced stress changes on a fault without offset were equivalent to the analytical solutions for poroelastic stress changes in laterally extensive reservoirs (e.g., Segall & Fitzgerald, 1998), the offset case locally resulted in a steeper stress path, a locally concentrated, more critical fault stress, and a lower pressure decrease required for reactivation. Using analytical solutions for poroelastic stressing within a reservoir to assess the fault reactivation potential will thus overestimate the critical pressure required for reactivation in a reservoir containing offset faults.

An increasing amount of elastic deformation of the fault prior to reactivation caused deviations from the analytical solutions for no offset faults and reduced the peakedness of stress concentrations for offset faults (see S3). Elastic deformation on the fault was controlled by the interface element stiffness, which could be used as a proxy for fault thickness. An alternative approach is to model the fault with ubiquitous joint elements, which have a finite thickness with a matrix that deform elastically or elastoplastically, and weak joint planes that can accommodate fault slip and weakening (Cappa & Rutqvist, 2012; Zbinden et al., 2017). Either way, care must be taken to set a realistic elastic deformation on the fault as it will influence the stress path and the pressure at which reactivation occurs. The stress concentrations may in part be artificial due to the sharp boundaries and linear elasticity prescribed to the depleting formations. Cores and outcrops show the boundaries between formations can be rather sharp (Buijze et al., 2017). Nonetheless, any form of deformation will (partly) relax the stress concentrations and cause a reduced and less sharp peak, as was observed for a low stiffness fault zone. If the damage zone surrounding the fault has a lower stiffness and accommodates more strain, the peakedness and amplitude of the stress concentrations could be reduced. Also, elastoplastic deformation of the fault zone and the reservoir can relax the stress concentrations.

Slip-weakening friction gave rise to a nucleation phase where a certain fault length was slipping aseismically, and subsequent instability of dynamic rupture. This resulted in extra pressure changes required for nucleation, for example, for a nucleation length of 10–20 m several MPa pressure change was required between reactivation and seismic instability. For ideal plastic fault behavior such a nucleation phase is lacking, and in several other studies the critical slip displacement was 1 or 2 orders smaller than the one used in the current study, so that the nucleation phase would have been much shorter, and the onset of reactivation and seismic instability much closer together (Cappa & Rutqvist, 2012; Zbinden et al., 2017). For modeling the timing of seismicity the potential existence of a nucleation phase may be very important, since several MPa depletion may correspond to years of production.

On the other hand, the reservoir thickness imposes a constraint on the maximum D_c and nucleation length; for D_c of centimeters the nucleation zone exceeded the reservoir thickness and no seismic instability could nucleate. Seismic instability also could not nucleate when D_c was reached before the critical nucleation length was attained. This occurred for very peaked stress concentrations. The uncertainty in the physics of the nucleation process of earthquakes, and (scaling of) D_c and the nucleation length is however significant.

4.2. Dynamic Rupture Propagation and Criterion for Runaway Ruptures

Most ruptures remained confined to the reservoir depth interval, but under some conditions rupture propagated into the overburden and underburden, or transitioned into a runaway rupture. A convenient parameter to study the propensity for (runaway) rupture propagation outside of the reservoir is the ratio between the stress drop and the strength drop $T = (\tau_0 - \tau_d)/(\tau_f - \tau_d$; e.g., Ripperger et al. 2007). This parameter is similar to, for example, the excess strength ratio S (Galis et al., 2015) with $T = 1/(1 + S)$, or to C which is defined as τ_d/τ_0 (Norbeck & Horne, 2018), and captures the effect of in situ stress and the friction drop on rupture potential. For $T < 0$ the τ_d is larger than τ_0 (i.e., negative stress drop), which inherently stabilizes and arrests rupture, and for $T > 0$ the fault is increasingly critical. To analyze the propensity for rupture to propagate into the overburden and underburden an average T was calculated for fault outside of the reservoir depth interval. Inside the reservoir T was variable as both the normal and shear stress changed during depletion; in the nucleation zone T was 1.

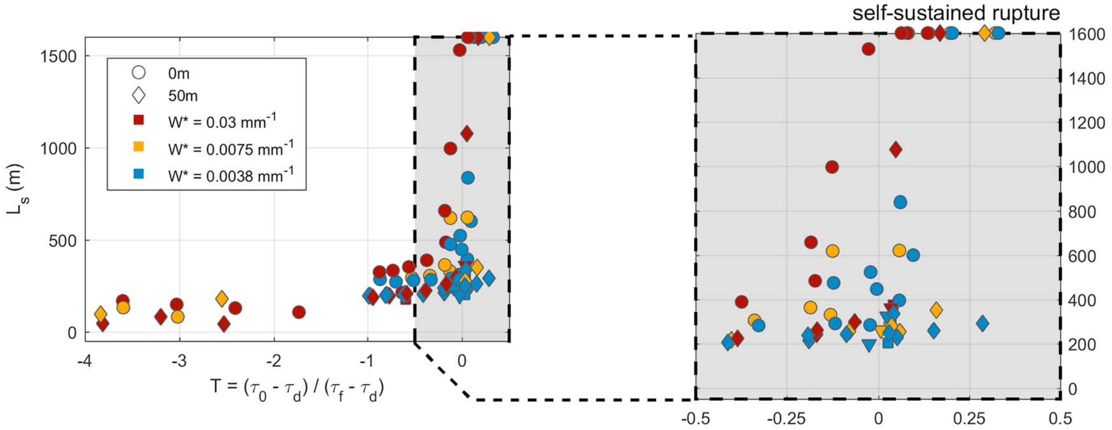

Figure 12. Rupture length L_s versus ratio of stress drop and strength drop $T = (\tau_0 - \tau_d)/(\tau_f - \tau_d)$. The T is the average value outside of the reservoir interval. The circles show no offset runs; the diamonds show 50-m offset runs. The colors indicate the different weakening rates W*. Ruptures plotted at 1,600-m rupture the entire fault.

The dynamic simulations showed a gradual transition from events smaller than or equal to the reservoir thickness to ruptures exiting the reservoir and runaway rupture (Figure 12). For $T < -0.2$ all ruptures were arrested within or within 100 m of the reservoir interval. For $-0.2 < T < 0$ the state of stress was still stable but closer to critical, which allowed for some propagation into the overburden and underburden even though the stress drop was negative or zero. In particular, for 0-m offset rupture could propagate to several hundreds of meters into the underburden; for the 50-m offset case rupture was arrested at the reservoir interval (L_s = ~200 m) due to the more heterogeneous stresses that developed during depletion. For $T > 0$ more ruptures propagated outside the reservoir interval and propagated several 100 m. Runaway rupture occurred at $T = 0.1$ for 0-m offset and high W* runs. A lower weakening rate W* of 0.0038 (larger D_c and larger fracture energy) decreased rupture length and shifted the transition to runaway rupture to higher T of 0.15–0.35, since more energy was consumed by the fracturing and less energy was available for propagation. Formation offset also lead to reduced rupture propagation, because stable stress areas formed along the fault at the reservoir top and bottom during depletion.

The findings are in agreement with criteria for runaway rupture in other studies but show also that increasing fracture energy and stress heterogeneity due to reservoir offset caused smaller ruptures and more diverse rupture sizes. For quasi-static and quasi-dynamic models with a critical slip distance $D_c \rightarrow 0$ slip will occur where $T > 0$ and will not occur where $T < 0$. A very sharp transition between arrested ruptures and runaway ruptures was observed at $C = 1$ ($T = 0$) for injection-induced ruptures with a D_c of 50 μm (Norbeck & Horne, 2018). When larger D_c are used the transition to runaway rupture will shift to higher T. In this study the transition was found at a T 0.05–0.15 for D_c = 0.005–0.04 m and fracture energy $G_c = 10^4$–10^5 Pa (Figure 12) Ripperger et al. (2007) observed the transition to runaway rupture at T 0.3–0.4 for a D_c = 0.2 m, $G_c = 1.8 \times 10^6$ Pa and also showed that a variable stress field as a result of roughness caused a more gradual transition to runaway rupture, with more distributed event sizes. Likewise, the presence of different reservoir offsets (and other heterogeneities) resulting in a heterogeneous fault stress caused a variable event sizes in our study, or in some cases could inhibit rupture propagation into the underburden even for high T. This shows the importance of incorporating (an approximation of) the depletion-induced stresses in the assessment of rupture propagation potential into the underburden.

In addition to the fracture energy and stress heterogeneity, also the size of the highly stressed zone where rupture nucleates can affect the transition to runaway ruptures. In fully dynamic simulations with artificial nucleation a relatively long critically stressed asperity with respect to the critical nucleation size promoted runaway rupture (Galis et al., 2015). For the reservoir geometry in our study this would imply thicker reservoir would create a higher potential for rupture propagation into the underburden, for the same friction parameters. We recommend to investigate the effect of reservoir thickness in future studies.

The shear stress ratio T can be a useful first-order indicator for rupture potential into the underburden, before starting a time-consuming dynamic rupture analysis. However, we showed how the critical slip distance (and fracture energy), and the depletion-induced stress distribution, also had a large influence on the rupture potential. We recommend future work on establishing a rupture arrest criterion, which incorporates the initial state of stress, stress drop, and fracture energy, and (an approximation of) stresses induced by reservoir depletion, and to validate it against dynamic simulations, cf., for example, Galis et al. (2017).

4.3. Limitations

In our modeling approach necessarily simplifications have been made. Here we discuss a number of the assumptions that are relevant for the modeled induced events.

The formations were modeled using linear elastic behavior. Recent experiments showed however that inelastic strain constituted a significant fraction of compaction strain in porous sandstones (Pijnenburg et al., 2018). Modeling reservoir compaction with elastoplastic or viscoelastic formation properties will cause a more stable stress path and fault reactivation at higher pressure changes. Also, the dynamic rupture characteristics will be affected, as off-fault plasticity will dissipate energy outside of the fault (e.g., Andrews, DJ, 2005). Further modeling efforts into elastoplastic reservoir behavior and its effect on the size of induced ruptures is recommended.

The imposed uniform pressure changes to simulate depletion and the one-way coupling with stress are simplifications. However, for a subsection of the Groningen a uniform gas pressure change may justified, as the observed pressure gradients across the field are small and most faults are not sealing and thus hold no or very little pressure differential. In other settings the pressure distribution may be more variable, and in that case it is important to include fully coupled flow models to simulate depletion. In particular, when pressure depletion in the fault zone is slower than in the reservoir because of low fault permeability the stress path can become more nonlinear and more unstable (Zbinden et al., 2017). On the other hand, depletion of the fault section in the underburden would reduce rupture potential into the underburden. Another assumptions concern the Biot coefficient, which was taken as 1.

Figure 7b showed that reactivation pressure increased strongly with decreasing the Biot coefficient, which mainly prevented nucleation on the 0-m offset fault. On the 50-m offset fault more pressure change was required for nucleation, but at nucleation the stress criticality on the fault was rather similar and may have limited effect on the rupture extent. However, further analysis of the effect of Biot coefficient on rupture size is advised for future work. Also, further research on the effect of coupled poroelasticity on dynamic rupture for faults in gas fields and the fluid-filled faults of the underburden is recommended, as coseismic poroelasticity may affect rupture velocity and size (Jin & Zoback, 2018).

Here we focused on the downdip rupture extent in a 2-D model geometry. Many gas reservoirs are laterally extensive, and hence, elongated stress concentrations will be expected along the fault's strike. The nucleation length in 2-D is likely similar to that in a 3-D case (Uenishi, 2018), but the along-strike dimension will be very important for the total ruptured area and seismic moment. We recommend further research on the rupture sizes that can be expected for dynamic rupture along elongated stress concentrations. Another effect of 2-D is the occurrence of supershear, which was observed in our models. Supershear can occur for Mode II ruptures only. In 3-D the rupture would be a mixture of Mode II (downdip) and Mode III (along-strike) propagation. This may affect the occurrence of supershear and the rupture length.

To model friction and rapid earthquake slip, a linear slip-weakening friction was used; a simplified model for fault slip used in many earthquake simulations. In laboratory experiments friction is often described as a function of velocity and time, by the rate and state friction model. Using rate and state friction can result in more pulse-like ruptures, which are different from the crack-like rupture observed in this study. Furthermore, rate-and-state friction leads to rate effects, which are not captured with slip-weakening, for example, the effect of loading rate on the critical nucleation length. This is interesting, as in this case the depletion rate may have an effect on the seismicity rate, which could lead to a different production strategy.

In general, our study showed that the rupture size was strongly affected by the assumed dynamic friction, which is a key parameter for both slip-weakening and rate-and-state friction behavior. However, the relevant in situ dynamic behavior of fault rocks in general is poorly known, and in particular, for small earthquakes the dynamic friction and dynamic weakening (and healing) mechanisms are poorly understood. Also, faults may have significant cohesion due to healing and cementation, especially the cataclastic faults in the Rotliegend formation of the Groningen field, which have been inactive for long periods of time.

Laboratory experiments indicate a significant strength gain with healing time, possibly even up to intact rock strength if healing time is long (Muhuri et al., 2003). This would strengthen the faults but also cause a larger stress drop when the fault breaks. Further understanding of the relevant frictional properties for small to moderate earthquakes on upper crustal faults is vital (Spiers et al., 2017).

4.4. Implications for Seismicity in Groningen

Dynamic rupture length increased for increasing strength ratio T that followed from the in situ stress state, and stress drop, which were both assumed uniform in the model. In and around the Groningen field, however, the state of stress and the stress drop may vary with depth because various stratigraphic units are present, which have different deformation properties. This will affect the rupture potential outside of the reservoir. The ~50-m-thick Ten Boer formation above the Rotliegend consists of clays and sandy material, which may have a higher horizontal stress due to creep (Sone & Zoback, 2014). The Triassic overburden (Zechstein Group) overlying the Groningen Slochteren sandstone and the Ten Boer is composed of a basal anhydrite and carbonate section of 50 m thick, overlain by hundreds of meters of rocksalt (e.g., de Jager & Visser, 2017). Creep of salt relaxes shear stresses and will create a near-isotropic state of stress over geological time, that is, a stress ratio K_0 of 1 and an initial shear stress $\tau_0 = 0$ (e.g., Haug et al., 2018). This isotropic stress is supported by near-lithostatic pore pressure measurements in the Zechstein (Verweij et al., 2012). A high K_0 will strongly reduce T and prevent propagation into the overburden (e.g., Buijze et al., 2017). Although upward propagation is thus prevented by the presence of salt, a local reduction in normal stress on offset faults just below the salt can locally promote failure (Haug et al., 2018; Orlic & Wassing, 2012). The presence of salt may thus lead to lower reactivation pressure than observed in our study but also lead to smaller dynamic ruptures compared to those in Figure 12.

Faults continue below the reservoir for at least several hundreds of meters into the Carboniferous underburden (Kortekaas & Jaarsma, 2017), which is composed of a tilted succession of shales, silts, and sandstone beds intercalated with coal seams (de Jager & Visser, 2017). No stress measurements have been conducted in the underburden. However, time-dependent deformation of clay-rich rocks is expected to relax a (significant) fraction of differential stress over geological time (Sone & Zoback, 2014). As the underburden is more clay-rich than the reservoir, the in situ horizontal stress is expected to be larger, resulting in a larger K_0 and smaller in situ shear stress. This in turn yields a lower T, making propagation into the underburden less favorable and lowering rupture sizes even further.

Also, wave propagation may be strongly influenced by velocity contrast between layers. For a low-velocity formation such as the Rotliegend in the Groningen field this may potentially trap a lot of seismic energy within the formation (Buijze et al., 2017). Note that here the elastic properties are equivalent for the quasi-static compaction phase and the dynamic rupture. In reality dynamic elastic properties can be different from the static elastic properties, which will affect wave propagation.

In the model the friction properties along the fault were uniform. However, as the faults crosscut different stratigraphic formations, the fault rock is expected to vary. Different fault rock mineralogies yield different fault strengths and frictional behavior (Hunfeld et al., 2017). The frictional strength and stress drop also strongly affect T and rupture size. Propagation into fault rocks with low frictional strength such as the clay-rich Ten Boer and underburden may be favorable. However, the velocity dependence of these rocks is likely stabilizing, and the expected stress drop under the conditions of rupture propagation at the in situ pressures and temperatures is highly uncertain. We recommend further research on the potential dynamic weakening of Groningen type fault rocks and include a broader range of uncertainties in future modeling.

The model results indicated that fault offset promoted fault reactivation. This is supported by the location of recent events the Groningen field, which could be located with greater accuracy due to the new monitoring network (Spetzler & Dost, 2017). Most of these events were mapped on known faults, that is faults that are visible on seismic because they offset the reservoir with a certain amount (>20 m). A relationship between earthquake occurrence and fault offset was however not (Wentinck, 2016), but within all the uncertainties in location of the earlier events a correlation may however be difficult. On the other hand, the results of this study also indicated that propagation into the underburden was more likely for small offset where no or only small parts of the faults became more stable during depletion. Larger events could occur, even for $T < 0$.

Interestingly enough, the largest magnitude events in the Groningen field seem to support this finding. The largest magnitude observed thus far is the 8 December 2012 M 3.6 Huizinge earthquake, with an estimated slip 0.07 m with a radius of 400 m based on a circular rupture (Dost & Kraaijpoel, 2013). Such a size could be confined to the reservoir, but this would require a very high aspect ratio. At first no fault was recognized at the hypocenter location, but recent improvements in the fault model showed a fault with small throw at the hypocenter location (Kortekaas & Jaarsma, 2017). Rupture into the underburden may thus have occurred for this event. Small offset faults are reactivated later in the lifetime of the field but may pose a larger hazard for rupture propagation.

4.5. Broader Implications for Modeling of Induced Seismicity

The dynamic model results showed that the stress distribution in and around the depleting reservoir had a strong effect on rupture length (see also section 4.2 and Figure 12). Some models relating operational parameters and the potential magnitude of induced seismicity do not consider explicitly the stress distribution (McGarr, 2014; Shapiro et al., 2011). These models also assume that the rupture remains confined to the interval affected by fluid injection. Although in most of our results rupture did remain confined to the reservoir interval, propagation outside of the reservoir interval also occurred. This was more likely for the smooth stress perturbation related to 0-m offset reservoir compartments, compared to the more heterogeneous stress that developed along offset faults. To estimate potential rupture sizes, the effect of a (geometry-specific) stress distribution must not be ignored.

Dynamic effects were also observed to be important for rupture size, with supershear causing additional propagation into the underburden (0-m offset) and triggering of the stress concentrations for the offset case. A previous study showed that for 0-m offset the rupture size computed in a fully dynamic analysis was 10% larger than in a (less computer-intensive) quasi-static analysis (Wassing et al., 2016), which may be an acceptable difference in the framework of all other uncertainties. For more heterogeneous fault stress the difference could be larger.

Deterministic modeling as done in this study thus involves parameters with significant uncertainties (in particular D_c, μ_d, and in situ stress) and simplifying assumptions on the physics governing induced seismic events. The results are subject to uncertainties and should not be used directly; rather, the modeled trends are of importance and give insight in the mechanics that plays a role in generating induced events. Extending the model approach to a more stochastic analysis including broader parameter ranges and validation against field observations is recommended as a next step.

5. Conclusions

We performed dynamic simulations of fault reactivation and seismic rupture induced by the depletion of two reservoir compartments crosscut by a fault with or without offset. The model geometry, formation and fault properties, and stress state were based on the Groningen reservoir, but were kept uniform for the reservoir and the underburden and overburden, to highlight the development of stresses during depletion. Note that these findings apply to relatively uniform depletion of a gas reservoir with faults that are not sealing. The in situ stress, weakening rate (through the dynamic friction and the critical slip distance), and reservoir offset were varied to study the effect on fault reactivation, and on the along-dip dynamic rupture length. Note that the absolute values of reactivation and rupture length are subject to uncertainties because some input parameters are poorly constrained. However, the modeling study showed the following main trends and findings:

1. The modeled poroelastic stress changes and pressure required for reactivation for depletion of 0-m offset reservoir compartments agreed with the analytical solutions for a stiff fault zone (>10 times the elastic properties of the medium). For fault zones with a lower stiffness the poroelastic stressing rates were lower than the analytically calculated rates, and more depletion was required for reactivation. This is not necessarily wrong or unphysical; in contrary, an interface stiffness smaller than the adjacent formations may account for the fault thickness and elastic deformation of the thicker fault.
2. Onset of fault slip occurs at a reservoir depletion pressure ΔP_r, which increased with the total horizontal in situ stress ratio K_0. Onset of fault slip was strongly promoted by with reservoir offset (for offsets smaller than reservoir thickness) due to shear stress peaks at the top of the HW and at the base of the FW reservoir.

3. Inclusion of linear slip-weakening friction required a critical nucleation length to be slipping aseismically, before seismic instability could nucleate. The nucleation length agreed with theoretical estimates. However, merging of two stress peaks could cause the nucleation length to deviate. Also, when the critical slip distance is reached, continued aseismic slip occurred and instability was suppressed.
4. The downdip rupture length L_s decreased for more stable in situ stress, smaller stress drop, and smaller weakening rate (which is equivalent to larger critical slip distance and larger fracture energy).
5. Whereas fault offset promoted the nucleation of rupture, it reduced the down-dip rupture size. Rupture arrest occurred at stable stress regions, which had formed during depletion. The smaller the offset on the other hand, the larger the potential for rupture propagation into the underburden.
6. Note that the previous findings apply to a normal faulting regime. For a strike-slip or reverse stress regime the poroelastic stress changes would stabilize the fault, although differential compaction across the fault could still cause local stress concentrations. However, overall stresses on the steeply dipping normal fault in a reverse stress regime do not favor large ruptures.
7. The stress ratio (stress drop/strength drop) of the under- and overburden provides a convenient measure for the propensity of rupture to propagate outside of the reservoir. A transition to runaway rupture (i.e. ruptures propagating far outside the reservoir interval) was observed for high enough stress ratio (> 0.1). A larger fracture energy and reservoir offset reduced the propensity for runaway ruptures, causing smaller ruptures and shifting the transition to runaway ruptures to higher stress ratios. However, for a negative stress ratio some propagation outside the reservoir interval could occur on faults with no or little offset. These results show the importance of the induced fault stresses on rupture. On the other hand, rupture can be arrested for positive stress drop. Rupture arrest is promoted by a large fracture energy and reservoir offset.

Acknowledgments

This research was in part funded by Nederlandse Aardolie Maatschappij BV (NAM) in the framework of research agreement UI49294 “Studies on Fault (re)activation and dynamic friction and failure behavior.” Part of the research has also been conducted within the framework of the M4ShaleGas project that was funded by the European Union's Horizon 2020 research and innovation program under grant agreement 640715. Furthermore, we thank all colleagues and friends at TNO, Utrecht University, Shell, Global Solutions B.V. and NAM for their support and discussions on modeling of earthquakes. In particular, we thank Gerd-Jan Schreppers from DIANA FEA BV for his support and helpful discussions. We would like to thank the two reviewers for their constructive feedback. The input file for the 2-D reservoir model in DIANA v10.1 is found in the supporting information.

References

Andrews, D. J. (1976). Rupture velocity of plane strain shear cracks. *Journal of Geophysical Research*, *81*, 5679–5687. https://doi.org/10.1029/JB081i032p05679

Andrews, D. J. (2005). Rupture dynamics with energy loss outside the slip zone. *Journal of Geophysical Research*, *110*, B01307. https://doi.org/10.1029/2004JB003191

Beach, A., Lawson Brown, J., Welbon, A. I., McCallum, J. E., Brockbank, P., & Knott, S. (1997). Characteristics of fault zones in sandstones from NW England: Application to fault transmissibility. *Geological Society, London, Special Publications*, *124*(1), 315–324. https://doi.org/10.1144/GSL.SP.1997.124.01.19

Ben-Zion, Y., & Rice, J. R. (1997). Dynamic simulations of slip on a smooth fault in an elastic solid. *Journal of Geophysical Research*, *102*(B8), 17,771–17,784.

Buijze, L., van den Bogert, P. A. J., Wassing, B. B. T., Orlic, B., & ten Veen, J. (2017). Fault reactivation mechanisms and dynamic rupture modelling of depletion-induced seismic events in a Rotliegend gas reservoir. *Netherlands Journal of Geosciences*, *96*(05), s131–s148. https://doi.org/10.1017/njg.2017.27

Cappa, F., & Rutqvist, J. (2012). Seismic rupture and ground accelerations induced by CO_2 injection in the shallow crust. *Geophysical Journal International*, *190*(3), 1784–1789. https://doi.org/10.1111/j.1365-246X.2012.05606.x

Childs, C., Manzocchi, T., Walsh, J. J., Bonson, C. G., Nicol, A., & Schöpfer, M. P. J. (2009). A geometric model of fault zone and fault rock thickness. *Journal of Structural Geology*, *31*(2), 117–127. https://doi.org/10.1016/j.jsg.2008.08.009

Day, S. M. (1982). Three-dimensional simulation of spontaneous rupture: The effect of nonuniform prestress. *Bulletin of the Seismological Society of America*, *72*(6A), 1881–1902.

Day, S. M., Dalguer, L. A., Lapusta, N., & Liu, Y. (2005). Comparison of finite difference and boundary integral solutions to three-dimensional spontaneous rupture. *Journal of Geophysical Research*, *110*, B12307. https://doi.org/10.1029/2005JB003813

de Jager, J., & Visser, C. (2017). Geology of the Groningen field—An overview. *Netherlands Journal of Geosciences*, *96*(05), s3–s15. https://doi.org/10.1017/njg.2017.22

DIANA 10.1 User Manual. (2016). Delft, Netherlands: DIANA FEA BV. Retrieved from https://dianafea.com/manuals/d101/Diana.html

Dost, B., & Kraaijpoel, D. (2013). *The August 16, 2012 earthquake near Huizinge (Groningen)*. De Bilt: KNMI.

Duan, B., & Oglesby, D. D. (2006). Heterogeneous fault stresses from previous earthquakes and the effect on dynamics of parallel strike-slip faults. *Journal of Geophysical Research*, *111*, B05309. https://doi.org/10.1029/2005JB004138

Dunham, E. M., Belanger, D., Cong, L., & Kozdon, J. E. (2011). Earthquake ruptures with strongly rate-weakening friction and off-fault plasticity, part 1: Planar faults. *Bulletin of the Seismological Society of America*, *101*(5), 2296–2307. https://doi.org/10.1785/0120100075

Fjaer, E., Holt, R. M., Horsrud, P., Raaen, A. M., & Risnes, R. (2008). *Petroleum related rock mechanics* (2nd ed.). Amsterdam and Oxford: Elsevier.

Fukuyama, E., & Madariaga, R. (1998). Rupture dynamics of a planar fault in a 3D elastic medium: Rate- and slip-weakening friction. *Bulletin of the Seismological Society of America*, *88*(1), 1–17.

Galis, M., Ampuero, J. P., Mai, P. M., & Cappa, F. (2017). Induced seismicity provides insight into why earthquake ruptures stop. *Science Advances*, *3*(12), eaap7528. https://doi.org/10.1126/sciadv.aap7528

Galis, M., Pelties, C., Kristek, J., Moczo, P., Ampuero, J., & Mai, P. M. (2015). On the initiation of sustained slip-weakening ruptures by localized stresses. *Geophysical Journal International*, *200*(2), 888–907.

Harris, R. A., & Day, S. M. (1997). Effects of a low-velocity zone on a dynamic rupture. *Bulletin of the Seismological Society of America*, *87*(5), 1267–1280.

Haug, C., Nüchter, J., & Henk, A. (2018). Assessment of geological factors potentially affecting production-induced seismicity in North German gas fields. *Geomechanics for Energy and the Environment*, *16*, 15–31. https://doi.org/10.1016/j.gete.2018.04.002

Hettema, M. H. H., Schutjens, P. M. T. M., Verboom, B. J. M., & Gussinklo, H. J. (2000). Production-induced compaction of a sandstone reservoir: The strong influence of stress path. *SPE Reservoir Evaluation and Engineering*, *August*.

Hough, S. E., & Page, M. (2016). Potentially induced earthquakes during the early twentieth century in the Los Angeles Basin. *Bulletin of the Seismological Society of America*, *106*(6), 2419–2435. https://doi.org/10.1785/0120160157

Hunfeld, L. B., Niemeijer, A. R., & Spiers, C. J. (2017). Frictional properties of simulated fault gouges from the seismogenic Groningen gas field under in situ P–T -chemical conditions. *Journal of Geophysical Research: Solid Earth*, *122*, 8969–8989. https://doi.org/10.1002/2017JB014876

Ida, Y. (1972). Cohesive force across the tip of a longitudinal-shear crack and Griffith's specific surface energy. *Journal of Geophysical Research*, *77*, 3796–3805. https://doi.org/10.1029/JB077i020p03796

Jin, L., & Zoback, M. D. (2018). Fully dynamic spontaneous rupture due to quasi-static pore pressure and Poroelastic effects: An implicit nonlinear computational model of fluid-induced seismic events. *Journal of Geophysical Research: Solid Earth*, *123*, 9430–9468. https://doi.org/10.1029/2018JB015669

Kortekaas, M., & Jaarsma, B. (2017). Improved definition of faults in the Groningen field using seismic attributes. *Netherlands Journal of Geosciences*, *96*(05), s71–s85. https://doi.org/10.1017/njg.2017.24

Kraaijpoel, D., & Dost, B. (2013). Implications of salt-related propagation and mode conversion effects on the analysis of induced seismicity. *Journal of Seismology*, *17*(1), 95–107. https://doi.org/10.1007/s10950-012-9309-4

Lapusta, N., Rice, J. R., Ben-Zion, Y., & Zheng, G. (2000). Elastodynamic analysis for slow tectonic loading with spontaneous rupture episodes on faults with rate-and state-dependent friction. *Journal of Geophysical Research*, *105*(B10), 23,765–23,789.

McGarr, A. (2014). Maximum magnitude earthquakes induced by fluid injection. *Journal of Geophysical Research: Solid Earth*, *119*, 1008–1019. https://doi.org/10.1002/2013JB010597

Muhuri, S. K., Dewers, T. A., Scott, T. E., & Reches, Z. (2003). Interseismic fault strengthening and earthquake-slip instability: Friction or cohesion? *Geology*, *31*(10), 881–884. https://doi.org/10.1130/G19601.1

Mulders, F. M. M. (2003). Modelling of stress development and fault slip in and around a producing gas reservoir. (Doctoral Thesis, Technical University of Delft).

Nagelhout, A. C. G., & Roest, J. P. A. (1997). Investigating fault slip in a model of an underground gas storage facility. *International Journal of Rock Mechanics and Mining Sciences*, *34*, 212.e1–212.e14.

NAM (2016). *Groningen Pressure Maintenance (GPM) study—Progress report February 2016*. Assen: NAM B.V.

Nielsen, S., Spagnuolo, E., Smith, S. A. F., Violay, M., Di Toro, G., & Bistacchi, A. (2016). Scaling in natural and laboratory earthquakes. *Geophysical Research Letters*, *43*, 1504–1510. https://doi.org/10.1002/2015GL067490

Norbeck, J. H., & Horne, R. N. (2018). Maximum magnitude of injection-induced earthquakes: A criterion to assess the influence of pressure migration along faults. *Tectonophysics*, *733*, 108–118. https://doi.org/10.1016/j.tecto.2018.01.028

Orlic, B., & Wassing, B. B. T. (2012). Modeling stress development and fault slip in producing hydrocarbon reservoirs overlain by rock salt caprocks. 46th US Rock Mechanics/Geomechanics Symposium.

Orlic, B., & Wassing, B. B. T. (2013). A study of stress change and fault slip in producing gas reservoirs overlain by elastic and viscoelastic caprocks. *Rock Mechanics and Rock Engineering*, *46*(3), 421–435. https://doi.org/10.1007/s00603-012-0347-6

Palmer, A. C., & Rice, J. R. (1973). The growth of slip surfaces in the progressive failure of over-consolidated clay. *Proceedings of the Royal Society of London A: Mathematical, Physical and Engineering Sciences*, *332*(1591), 527–548. https://doi.org/10.1098/rspa.1973.0040

Pampillón, P., Santillán, D., Mosquera, J. C., & Cueto-Felgueroso, L. (2018). Dynamic and quasi-dynamic modeling of injection-induced earthquakes in poroelastic media. *Journal of Geophysical Research: Solid Earth*, *123*, 5730–5759. https://doi.org/10.1029/2018JB015533

Pijnenburg, R. P. J., Verberne, B. A., Hangx, S. J. T., & Spiers, C. J. (2018). Deformation behavior of sandstones from the seismogenic Groningen gas field: Role of inelastic versus elastic mechanisms. *Journal of Geophysical Research: Solid Earth*, *123*, 5532–5558. https://doi.org/10.1029/2018JB015673

Ripperger, J., Ampuero, J., Mai, P. M., & Giardini, D. (2007). Earthquake source characteristics from dynamic rupture with constrained stochastic fault stress. *Journal of Geophysical Research*, *112*, B04311. https://doi.org/10.1029/2006JB004515

Roest, J. P. A., & Kuilman, W. (1994) Geomechanical analysis of small earthquakes at the Eleveld gas reservoir.

Sanz, P. F., Lele, S. P., Searles, K. H., Hsu, S.-Y., Garzon, J. L., Burdette, J. A., et al. (2015). Geomechanical analysis to evaluate production-induced fault reactivation at Groningen gas field. In *SPE Annual Technical Conference and Exhibition*. Society of Petroleum Engineers.

Segall, P. (1985). Stress and subsidence resulting from subsurface fluid withdrawal in the epicentral region of the 1983 Coalinga earthquake. *Journal of Geophysical Research*, *90*, 6801–6816. https://doi.org/10.1029/JB090iB08p06801

Segall, P. (1989). Earthquakes triggered by fluid extraction. *Geology*, *17*(10), 942–946. https://doi.org/10.1130/0091-7613(1989)017<0942:ETBFE>2.3.CO;2

Segall, P., & Fitzgerald, S. D. (1998). A note on induced stress changes in hydrocarbon and geothermal reservoirs. *Tectonophysics*, *289*(1-3), 117–128. https://doi.org/10.1016/S0040-1951(97)00311-9

Segall, P., Grasso, J. R., & Mossop, A. (1994). Poroelastic stressing and induced seismicity near the Lacq gas field, southwestern France. *Journal of Geophysical Research*, *99*, 15,423–15,438. https://doi.org/10.1029/94JB00989

Shapiro, S., Krüger, O., Dinske, C., & Langenbruch, C. (2011). Magnitudes of induced earthquakes and geometric scales of fluid-stimulated rock volumes. *Geophysics*, *76*(6), WC55–WC63. https://doi.org/10.1190/geo2010-0349.1

Sone, H., & Zoback, M. D. (2014). Time-dependent deformation of shale gas reservoir rocks and its long-term effect on the in situ state of stress. *International Journal of Rock Mechanics and Mining Sciences*, *69*, 120–132.

Spiers, C. J., Hangx, S. J., & Niemeijer, A. R. (2017). New approaches in experimental research on rock and fault behaviour in the Groningen gas field. *Netherlands Journal of Geosciences*, *96*(5), s55–s69.

Spetzler, J., & Dost, B. (2017). Hypocentre estimation of induced earthquakes in Groningen. *Geophysical Journal International*, *209*(1), 453–465.

Uenishi, K. (2018). Three-dimensional fracture instability of a displacement-weakening planar interface under locally peaked nonuniform loading. *Journal of the Mechanics and Physics of Solids*, *115*, 195–207.

Uenishi, K., & Rice, J. R. (2003). Universal nucleation length for slip-weakening rupture instability under nonuniform fault loading. *Journal of Geophysical Research*, *108*(B1), 2042. https://doi.org/10.1029/2001JB001681

Urpi, L., Rinaldi, A. P., Rutqvist, J., Cappa, F., & Spiers, C. J. (2016). Dynamic simulation of CO_2-injection-induced fault rupture with slip-rate dependent friction coefficient. *Geomechanics for Energy and the Environment*, *7*, 47–65.

van den Bogert, P. A. J. (2015). Impact of various modelling options on the onset of fault slip and fault slip response using 2-dimensional finite-element modelling. *Restricted*, *Report No. SR.15.11455*, *Rijswijk: Shell Global Solutions International B.V*.

van Eijs, R. M. H. E. (2015). Neotectonic stresses in the Permian Slochteren Formation of the Groningen Field. *KNMI Scientific Report*, *Report No. EP201510210531*, *Assen: NAM*.

van Oeveren, H., Valvatne, P., Geurtsen, L., & van Elk, J. (2017). History match of the Groningen field dynamic reservoir model to subsidence data and conventional subsurface data. *Netherlands Journal of Geosciences*, *96*(05), s47–s54. https://doi.org/10.1017/njg.2017.26

van Thienen-Visser, K., Pruiksma, J. P., & Breunese, J. N. (2015). Compaction and subsidence of the Groningen gas field in the Netherlands. *Proceedings International Association of Hydrological Sciences*, *372*, 367–373.

Verweij, J. M., Simmelink, H. J., Underschultz, J., & Witmans, N. (2012). Pressure and fluid dynamic characterisation of the Dutch subsurface. *Netherlands Journal of Geosciences*, *91*(04), 465–490. https://doi.org/10.1017/S0016774600000342

Viesca, R. C., & Rice, J. R. (2012). Nucleation of slip-weakening rupture instability in landslides by localized increase of pore pressure. *Journal of Geophysical Research*, *117*, B03104. https://doi.org/10.1029/2011JB008866

Wassing, B. B. T., Buijze, L., & Orlic, B. (2016). Modelling of fault reactivation and fault slip in producing gas fields using a alip-weakening friction law American Rock Mechanics Association.

Wassing, B. B. T., Buijze, L., & Orlic, B. (2017). Fault reactivation and fault rupture in producing gas fields with elastic and visco-elastic caprocks. *51st Rock Mechanics Symposium San Francisco*, *ARMA 17-355*

Wentinck, R. H. (2015). Induced seismicity in the Groningen field—Statistical assessment of tremors along faults in a compacting reservoir. *Report No. SR.15.11335*, *Rijswijk: Shell Global Solutions International B.V*.

Wentinck, R. H. (2016). *Induced seismicity in the Groningen field: Second statistical assessment of tremors along faults in a compacting reservoir*. Assen: Nederlandse Aardolie Maatschappij B.V.

Yerkes, R. F., & Castle, R. O. (1976). Seismicity and faulting attributable to fluid extraction. *Engineering Geology*, *10*(2–4), 151–167. https://doi.org/10.1016/0013-7952(76)90017-X

Zbinden, D., Rinaldi, A. P., Urpi, L., & Wiemer, S. (2017). On the physics-based processes behind production-induced seismicity in natural gas fields. *Journal of Geophysical Research: Solid Earth*, *122*, 3792–3812. https://doi.org/10.1002/2017JB014003